

Precise predictions for same-sign W-bosons scattering at the LHC

Alessandro Ballestrero⁸, Benedikt Biedermann¹, Simon Brass², Ansgar Denner¹, Stefan Dittmaier³, Pietro Govoni⁴, Michele Grossi^{5,6}, Alexander Karlberg⁷, Ezio Maina^{8,9}, Mathieu Pellen¹, Giovanni Pelliccioli^{8,9}, Simon Plätzer¹⁰, Michael Rauch¹¹, Jürgen Reuter¹², Vincent Rothe¹², Christopher Schwan³, Pascal Stenemeier¹², Marco Zaro¹³

¹Universität Würzburg, Institut für Theoretische Physik und Astrophysik, Emil-Hilb-Weg 22, 97074 Würzburg, Germany

²Universität Siegen, Department Physik, Walter-Flex-Str.3, 57068 Siegen, Germany

³Albert-Ludwigs-Universität Freiburg, Physikalisches Institut, Hermann-Herder-Str. 3, 79104 Freiburg, Germany

⁴Milan, Italy

⁵Università di Pavia, Dipartimento di Fisica and INFN, Sezione di Pavia, Via A. Bassi 6, 27100 Pavia, Italy

⁶IBM Italia s.p.a. Circonvallazione Idroscalo, 20090 Segrate (MI), Italy

⁷Department of Physics, University of Zürich, CH-8057 Zürich, Switzerland

⁸INFN, Sezione di Torino, Via P. Giuria 1, 10125 Torino, Italy

⁹Università di Torino, Dipartimento di Fisica, Via P. Giuria 1, 10125 Torino, Italy

¹⁰Particle Physics, Faculty of Physics, University of Vienna, Vienna, Austria

¹¹Institute for Theoretical Physics, Karlsruhe Institute of Technology (KIT), Karlsruhe, Germany

¹²DESY Theory Group, Notkestr. 85, D-22607 Hamburg, Germany

¹³Nikhef, Science Park 105, 1098XG Amsterdam, The Netherlands

the date of receipt and acceptance should be inserted later

Abstract

In this article, a detailed study of the vector-boson scattering for two positively charged W bosons is presented. In particular, a comparison between the full next-to-leading (NLO) QCD corrections against several approximations is carried out. This study is not only performed in the usual fiducial region used by experimental collaborations but also in a more inclusive set-up. This allows to infer precisely the quality of such approximations. Finally, NLO predictions matched to various parton shower are also discussed. Thanks to this, it is thus possible to infer the systematic errors related to vector-boson scattering at the NLO-QCD level and beyond.

1 Introduction

Vector-boson scattering (VBS) is a class of processes that allow to probe the nature of Higgs-vector-vector couplings and quartic gauge couplings. It is usually understood that VBS refers to the scattering of massive vector-bosons (W^\pm, Z), which therefore couple to the Higgs boson and can be longitudinally polarized. The scattering of longitudinally polarized bosons is of particular interest, because the corresponding matrix elements feature both gauge and unitarity cancellations that strongly depend on the actual form of the Higgs sector. A detailed study of this class of processes will therefore further constrain the Higgs couplings and hint at or exclude non-Standard Model Higgs bosons.

The process with two positively charged W bosons is the VBS process with the largest signal-to-background ratio at the LHC, for which evidence has been found in 8 TeV data [1, 2] and which is now started to be observed [3] and measured [4] in 13 TeV data. For now the measurements of VBS processes are limited by statistics but the situation will change in a near future. On the theoretical side, it is thus of prime importance to provide precise predictions and infer their related systematic errors.

The W^+W^+ scattering is the simplest VBS process to calculate, because of the double-charge structure of

the leptonic final state that limits the number of partonic processes and total number of Feynman diagrams for each process. It also implies that irreducible backgrounds are comparatively small, which make this VBS process experimentally favourable in comparison to *e.g.* to W^+W^- scattering, which has the largest cross section. Therefore, the W^+W^+ scattering is an ideal candidate for a detailed study of various theoretical predictions.

In the last few years, several leading order (LO) and next-to-leading order (NLO) computations became available for both the VBS process [5–8] and its QCD-induced irreducible background process [8–12]. These computations all rely on approximations, while recently the complete NLO corrections have been performed [13]. It is therefore interesting to infer in details the quality of the various approximations. Indeed, apart from Ref. [13] where it is commented on, [MP: more references?] no detailed comparison of the VBS approximations have been carried out. Preliminary results have already been made public in Ref. [14].

The hadronic process is $pp \rightarrow \mu^+\nu_\mu e^+\nu_e jj + X$, which includes the W^+W^+ scattering. This final state possesses three contributions at LO whose coupling orders are $\mathcal{O}(\alpha^6)$, $\mathcal{O}(\alpha_s\alpha^5)$, and $\mathcal{O}(\alpha_s^2\alpha^4)$. They are commonly referred to as electroweak (EW), interference, and QCD contributions, respectively.¹ Therefore, the present work starts with a LO study of these three contributions as a function of typical VBS cuts. This allows to quantify the various contributions to the final state $\mu^+\nu_\mu e^+\nu_e jj$. This is followed by a LO comparison between the various predictions at the level of the cross section and differential distributions.

At NLO, the process possesses four contributions of orders $\mathcal{O}(\alpha^7)$, $\mathcal{O}(\alpha_s\alpha^6)$, $\mathcal{O}(\alpha_s^2\alpha^5)$, and $\mathcal{O}(\alpha_s^3\alpha^4)$. The largest ones are the EW corrections [13, 15] of order $\mathcal{O}(\alpha^7)$. The contribution to the order $\mathcal{O}(\alpha_s\alpha^6)$ is the second largest NLO contribution and is often referred to as the QCD corrections to the VBS process. In the following, this order is the one where our comparisons are focused on. In this article we will refer to it as simply *NLO*. As for the LO study, the various predictions are compared at the level of the cross section and differential distributions. In particular, this allows to infer the accuracy of the so-called VBS approximation, which we will define in more detail later. To our knowledge, such a detailed study was still missing.

Finally, several predictions featuring parton shower are compared. This allows to infer systematic differences between the various predictions. This is the first

time in the literature that such an analysis has been carried out [MP: True?] .

Obviously all VBS processes deserve such a detailed study but the present article sets standards for inferring systematics related to NLO corrections and beyond.

The article is organised as follow: in Sec. 2 the studied process is defined. Various approximation at LO and NLO are described in Sec. 3. This is followed by a presentation of the programs used for the computations. Sections 4 and 5 are devoted to a LO and NLO study, respectively. Section 6 deals with the matching to parton shower. The last section consists in concluding remarks and recommendations for experimental collaborations.

2 Definition of the process

The scattering of two positively charged W bosons is proceeding at the LHC through the partonic process:

$$pp \rightarrow \mu^+\nu_\mu e^+\nu_e jj + X. \quad (1)$$

This process possesses three LO contributions of different orders. The first one is of order $\mathcal{O}(\alpha^6)$ and is referred to as EW contribution. In addition to typical VBS contributions, as shown on the left of Fig. 1, it also features *s*-channel contributions. Note that we define *s*-, *t*-, and *u*-channel contributions by looking at the process which is contained by only looking at the quark lines. The *s*-channels will play a particular role in the study of the various contributions in Sec. 4.1. Some of them take the form of decay chains, for example the diagram represented in the middle of Fig. 1, while others are tri-boson contributions (right of Fig. 1). The VBS diagrams typically dominate the full process. But all these contributions form a single gauge-invariant set of contributions and therefore cannot be separated.

The process can also be mediated via a gluon connecting the two quark lines while the W bosons are radiated off the quark lines. These contributions are of order $\mathcal{O}(\alpha_s^2\alpha^4)$ and feature different kinematical behaviours than the EW contribution. Nonetheless they share the same final state and therefore constitute an irreducible background.

Finally, due to the specific colour structure of these two classes of amplitudes, there exist non-zero interferences if only one quark family is involved. These are of order $\mathcal{O}(\alpha_s\alpha^5)$ and are usually small but not negligible for realistic experimental set-ups [13].

In experimental measurements, special VBS-cuts are designed to enhance the EW contribution over the QCD one. These cuts are based on the fact that the two contributions have different kinematical behaviour. The

¹The EW contribution is sometimes referred to as the VBS contribution even it possesses non-VBS contributions.

EW contribution is characterised by two jets with large rapidities as well as a large invariant mass. The two W bosons are mostly produced centrally. This is in contrast to the QCD contribution which favours jets in the central region. Therefore, the event selection usually involves rapidity-difference and invariance-mass cuts for the jets. This will also be discussed in Sec. 4.1.

3 Details of the calculations

3.1 Several descriptions for one process

As mentioned previously, the EW contribution is dominated by the scattering of two W gauge bosons. Therefore it is justified to approximate the full EW contributions simply by the VBS contributions. Nonetheless, this set of contributions is not gauge invariant. To make it gauge-invariant, one should project on-shell the incoming W boson. Unfortunately, this momentum is space-like and thus a simple on-shell projection is not possible. Instead, one can keep the W boson leg connected to the external quark line off-shell while the one connected to the scattering is put on-shell. Then the polarisation of the gauge boson is accommodated following the implementations of Refs. [16, 17]. Such an approximation is usually called effective vector-boson approximation (EVBA) [18–20].

A less crude approximation consists in considering all t - and u - diagrams and squaring them separately and neglecting their interferences. These interferences are expected to be small in the VBS fiducial region. The s -channel squared diagrams and interferences with s -channels are left out as well. This approximation is often called t -/ u - approximation, VBF, or even VBS approximation. We will adopt the latter denomination in the following of the article. Such an approximation is implemented at LO in the computer codes BONSAY and POWHEG. This approximation is gauge-invariant, which can be seen by considering the quark coming from different protons belonging to different $SU(3)$ gauge groups.

The squared matrix element of the s -channel contributions can added back, but all interferences between different kinematic channels are still neglected. This is what is done in VBFNLO.

All other codes (MG5_AMC, MoCANLO+RECOLA, PHANTOM, and WHIZARD) consider all contributions of order $\mathcal{O}(\alpha^6)$ as well as all possible interferences. Note that the final W boson can always be considered either on-shell or off-shell without affecting the previous discussion. All the codes mentioned here are described in details in the following sub-section.

Moving on to NLO accuracy, one can extend the approximations presented at LO. The VBS approximation at NLO is straightforward for the virtual contributions, for the real-contributions one must be careful about gluon-initiated processes². This is implemented in POWHEG. This approximation can be used in combination with a double-pole approximation [21] for the virtual contribution. Such an approximation is implemented in BONSAY. In VBFNLO, the VBS approximation at NLO with s -channel contributions is implemented.

A further refinement is to consider the full real contributions as well as part of the virtual. In particular one can consider only one-loop amplitudes where there is no gluon exchange between the quarks and assuming a cancellation of the infrared (IR) poles. [MP: True? I cannot remember exactly what is included] . Such predictions are provided by MG5_AMC.

Finally the full $\mathcal{O}(\alpha_s\alpha^6)$ computation consists also of EW corrections in the virtual as well as real corrections [13]. Such predictions are provided by the combination MoCANLO+RECOLA as published in Ref. [13].

In Tab. 1 the details of the various codes are reported. In particular, it is specified whether

- all s - and t/u -channel diagrams that lead to the considered final state are included;
- interferences between diagrams are included at LO;
- diagrams which do not feature two resonant vector bosons are included;
- the so-called non-factorisable (NF) QCD corrections, that is the corrections where (real or virtual) gluons are exchanged between different quark lines, are included;
- EW corrections to the $\mathcal{O}(\alpha^5\alpha_s)$ interference are included. These corrections are of the same order as the NLO QCD corrections to the $\mathcal{O}(\alpha^6)$ term.

3.2 Description of the predictions

In the comparison, the following codes are used:

- The program BONSAY consists of a general-purpose Monte Carlo integrator and matrix elements taken from several sources. Born matrix elements are adapted from the program LUSIFER [22] for the partonic

²The initial gluon must not couple to the other initial quark, otherwise there are infrared divergences proportional to s -channels which do not match with the ones found in the virtual contributions. The subset of diagrams where all couplings of the initial state gluon to initial state quark are neglected forms a gauge-invariant subset, with the same argument as presented above.

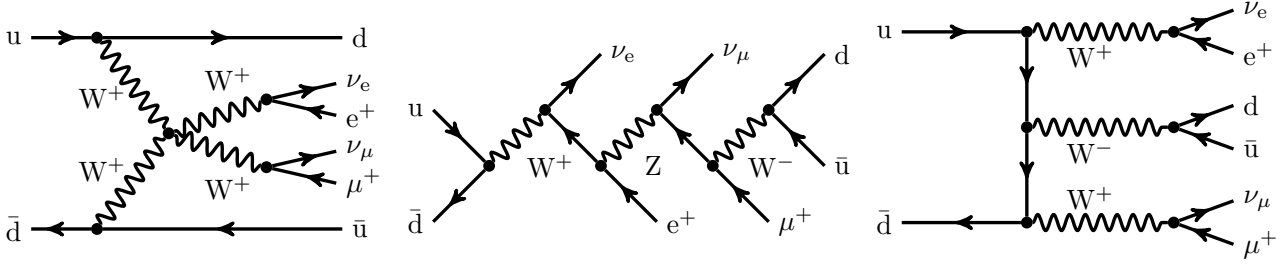


Fig. 1: Sample tree-level diagrams that contribute to the process $pp \rightarrow \mu^+\nu_\mu e^+\nu_e jj$ at order $\mathcal{O}(\alpha^6)$. In addition to typical VBS contribution (left), this order also possesses s -channel (middle) and tri-boson contributions (right).

Code	$\mathcal{O}(\alpha^6) s ^2/ t ^2/ u ^2$	$\mathcal{O}(\alpha^6)$ interf.	Non-res.	NLO	NF QCD	EW corr. to $\mathcal{O}(\alpha_s\alpha^5)$
BONSAY	t/u	No	Yes, virt. No	Yes	No	No
POWHEG	t/u	No	Yes	Yes	No	No
MG5_AMC	Yes	Yes	Yes	Yes	No virt.	No
MoCANLO+RECOLA	Yes	Yes	Yes	Yes	Yes	Yes
PHANTOM	Yes	Yes	Yes	No	-	-
VBFNLO	Yes	No	Yes	Yes	No	No
WHIZARD	Yes	Yes	Yes	No	-	-

Table 1: Summary of the different properties of the codes employed in the comparison.

processes, real matrix elements are written by Marina Billoni, and virtual matrix elements by Stefan Dittmaier. One loop integrals are evaluated using the COLLIER library [23, 24].

- MADGRAPH5_AMC@NLO [25] is an automatic meta-code (a code that generates codes) which makes it possible to simulate any scattering process including NLO QCD corrections both at fixed order and including matching to parton showers. It makes use of the FKS subtraction method [26, 27] (automated in the module MADFKS [28, 29]) for regulating IR singularities. The computations of one-loop amplitudes are carried out by switching dynamically between two integral-reduction techniques, OPP [30] or Laurent-series expansion [31], and TIR [32–34]. These have been automated in the module MADLOOP [35], which in turn exploits CUTTOOLS [36], NINJA [37, 38], or IREGI [39], together with an in-house implementation of the OPENLOOPS optimisation [40].

The simulation of VBS at NLO-QCD accuracy can be performed by issuing the following commands in the program interface:

```
> set complex_mass_scheme #1
> import model loop_qcd_qed_sm_Gmu #2
> generate p p > e+ ve mu+ vm j j QCD=0 [QCD] #3
> output #4
```

With these commands the complex-mass scheme is turned on #1, then the NLO-capable model is loaded

#2³, finally the process code is generated #3 (note the QCD=0 syntax to select the purely-electroweak process) and written to disk #4. Because of some internal limitations, which will be lifted in the future version capable of computing both QCD and EW corrections, only loops with QCD-interacting particles are generated. [MP: Detail of the approximation done, divergent part, assumed to cancel etc.]

- PHANTOM [41] is a dedicated tree-level Monte Carlo for six parton final states at pp, p \bar{p} and e $^+e^-$ colliders at orders α^6 and $\alpha_s^2\alpha^4$ including interferences between the two sets of diagrams. It employs complete tree-level matrix elements in the complex-mass scheme [42] computed via the modular helicity formalism [43, 44]. The integration uses a multichannel approach [45] and an adaptive strategy [46]. PHANTOM generates unweighted events at parton level for both the SM and a few instances of BSM theories.
- The POWHEG-BOX [47, 48] is a framework for matching NLO-QCD calculations with parton showers. It relies on the user providing the matrix elements and Born phase space, but will automatically construct FKS [26] subtraction terms and the phase space for the real emission. For the VBS processes all matrix elements are being provided by a previous version

³Despite the loop_qcd_qed_sm_Gmu model also includes NLO counterterms for computing electro-weak corrections, it is not yet possible to compute such corrections with the current version of the code.

of VBFNLO [49, 50, 12] and hence the approximations used in the POWHEG-BOX are the similar to those used in VBFNLO. [MP: Mention the non-clustering for the scale as well as the different running of alphas at NLO.]

- The program MoCANLO+RECOLA is made of a flexible Monte Carlo program dubbed MoCANLO and of the general matrix element generator RECOLA [51, 52]. The fast integration is ensured by using similar phase-space mappings to those of Refs. [53, 54, 22]. The IR divergences appearing in the real corrections are handles with the help of the Catani–Seymour dipole formalism [55, 56]. To numerically evaluate the one-loop scalar and tensor integrals, RECOLA relies on the COLLIER library [23, 24]. These tools have been successfully used for the computation of NLO corrections for high-multiplicity processes and in particular VBS [15, 13].
- VBFNLO [49, 50, 12] is a flexible parton-level Monte Carlo for processes with electroweak bosons. It allows the calculation of VBS processes at NLO QCD in the VBF approximation and including the s-channel triboson contribution, neglecting interferences between the two. Besides the SM, also anomalous couplings of the Higgs and gauge bosons can be simulated.
- WHIZARD [57, 58] is a multi-purpose event generator with the LO matrix element generator O’MEGA. It provides FKS subtraction terms for any NLO process, while virtual matrix elements are provided externally by OPENLOOPS [40] (alternatively, RECOLA [51, 52] (cf. above) can be used as well). WHIZARD allows to simulate a huge number of BSM models as well, in particular for new physics in the VBS channel in terms of both higher-dimensional operators as well as explicit resonances.

3.3 Input parameters

The VBS production mechanism is simulated at the LHC with a center-of-mass energy $\sqrt{s} = 13$ TeV. The NNPDF 3.0 parton density [59] with five flavour scheme, NLO QCD evolution, and a strong coupling constant $\alpha_s(M_Z) = 0.118$ is employed.⁴ Since the employed PDF set has no photonic density, photon-induced processes are not considered. Initial-state collinear singularities are factorised with the $\overline{\text{MS}}$ scheme, consistently with what is done in NNPDF.

⁴The corresponding `lhaid` in LHAPDF6 [60] is 260000.

For the mass and width of the massive particles, the following values are used:

$$\begin{aligned} m_t &= 173.21 \text{ GeV}, & \Gamma_t &= 0 \text{ GeV}, \\ M_Z^{\text{OS}} &= 91.1876 \text{ GeV}, & \Gamma_Z^{\text{OS}} &= 2.4952 \text{ GeV}, \\ M_W^{\text{OS}} &= 80.385 \text{ GeV}, & \Gamma_W^{\text{OS}} &= 2.085 \text{ GeV}, \\ M_H &= 125.0 \text{ GeV}, & \Gamma_H &= 4.07 \times 10^{-3} \text{ GeV}. \end{aligned} \quad (2)$$

The measured on-shell (OS) values for the masses and widths of the W and Z bosons are converted into pole values for the gauge bosons ($V = W, Z$) according to Ref. [61],

$$\begin{aligned} M_V &= M_V^{\text{OS}} / \sqrt{1 + (\Gamma_V^{\text{OS}} / M_V^{\text{OS}})^2}, \\ \Gamma_V &= \Gamma_V^{\text{OS}} / \sqrt{1 + (\Gamma_V^{\text{OS}} / M_V^{\text{OS}})^2}. \end{aligned} \quad (3)$$

The EW coupling is renormalised in the G_μ scheme [62] where

$$G_\mu = 1.16637 \times 10^{-5} \text{ GeV}^{-2}. \quad (4)$$

The numerical value of α , corresponding to the choice of input parameters is

$$\alpha = 7.555310522369 \times 10^{-3}. \quad (5)$$

The CKM-Matrix is assumed to be diagonal, meaning that we neglect mixing between different quark families. The complex-mass scheme [54, 63] is used throughout to treat unstable intermediate particles in a gauge-invariant manner.

The renormalisation and factorisation scales are set to the dynamical scale

$$\mu_{\text{ren}} = \mu_{\text{fac}} = \sqrt{p_{\text{T},j1} p_{\text{T},j2}}. \quad (6)$$

This choice of scale has been shown to provide stable NLO predictions [7].

Following experimental measurements [1, 4, 2, 64], the event selection used in the present study is:

- The two same-sign charged leptons are required to have

$$p_{\text{T},\ell} > 20 \text{ GeV}, \quad |y_\ell| < 2.5, \quad \Delta R_{\ell\ell} > 0.3. \quad (7)$$

- The total missing transverse energy, computed from the vectorial sum of the transverse momenta of the two neutrinos, is required to be

$$E_{\text{T,miss}} = p_{\text{T,miss}} > 40 \text{ GeV}. \quad (8)$$

- QCD partons (quarks and gluons) are clustered together using the anti- k_T algorithm [65] with distance parameter $R = 0.4$. Jets are required to have

$$p_{T,j} > 30 \text{ GeV}, \quad |y_j| < 4.5, \quad \Delta R_{j\ell} > 0.3. \quad (9)$$

Typically, on the two jets with largest transverse-momentum VBS cuts are applied. These are an invariant-mass cut on the di-jet system as well as rapidity-separation cut between the two jets. The nominal value of these cuts if not stated explicitly read:

$$m_{jj} > 500 \text{ GeV}, \quad |\Delta y_{jj}| > 2.5. \quad (10)$$

- When EW corrections are computed, real photons and charged fermion are clustered together using the anti- k_T algorithm with radius parameter $R = 0.1$. In this case, leptons and quarks are understood as *dressed fermions*.

4 Leading-order study

4.1 Three contributions

At tree level, there are three contributions to the W^+W^+ production in association with two jets: the pure EW component $\mathcal{O}(\alpha^6)$, the interference $\mathcal{O}(\alpha_s\alpha^5)$, and the QCD background $\mathcal{O}(\alpha_s^2\alpha^4)$. In the present section, the cross sections and distributions are obtained without applying the VBS cuts on m_{jj} and $|\Delta y_{jj}|$. In Tab. 2, the cross sections of the three contributions are displayed. The EW, QCD, and interference contributions amount to 57%, 37%, and 6% of the total inclusive cross section, respectively. The QCD contribution does not possess external gluons due to charge conservation. Thus the $\mathcal{O}(\alpha_s^2\alpha^4)$ diagrams only involve gluon exchange in the t/u -channel between the quark lines. This results in a small contribution although the VBS cuts have not been imposed. The interference between EW and QCD contributions is small, due to color suppression, but not negligible (t/u interference with identical fermions).

Order	$\mathcal{O}(\alpha^6)$	$\mathcal{O}(\alpha_s^2\alpha^4)$	$\mathcal{O}(\alpha_s\alpha^5)$
$\sigma[\text{fb}]$	2.292 ± 0.002	1.477 ± 0.001	0.223 ± 0.003

Table 2: Cross sections at LO accuracy for the $pp \rightarrow \mu^+\nu_\mu e^+\nu_e jj$ process. These results are for the set-up described in Sec. 3.3, dropping the m_{jj} and $|\Delta y_{jj}|$ cuts.

In Fig. 2 these three contributions are shown separately and summed in the differential distribution of the di-jet invariant mass m_{jj} and the rapidity difference $|\Delta y_{jj}|$. The EW contribution peaks around an invariant

mass of about 80 GeV. These are due to diagrams where the two jets originate from the decay of a W boson (see middle and right diagrams in Fig. 1). Note that these contributions are not present in calculations relying on the VBS approximation. Also, the EW contribution becomes dominant for di-jet invariant mass larger than 500 GeV and for jet rapidity difference larger than 2.5.

This can also be seen in Fig. 3 where the three contributions are displayed as a function of the di-jet invariant mass and jet rapidity difference. Again, it is obvious that the region with low di-jet invariant mass and low jet-rapidity difference should be avoided. This motivates in particular the choice of $m_{jj} > 200 \text{ GeV}$ and $|\Delta y_{jj}| > 2$ for our inclusive study (see below). Finally, let us notice that the choice $m_{jj} > 500 \text{ GeV}$ and $|\Delta y_{jj}| > 2.5$ made by the experimental collaborations is well motivated in order to enhance the EW contribution over its irreducible backgrounds. These are the cuts used in Sec. 4.3.

4.2 Inclusive comparison

As explained previously, the low di-jet invariant mass and low jet rapidity separation is dominated by tri-boson production. Therefore a comparison of the various approximations in an *inclusive* phase-space volume is performed. To that end, we have chosen for the inclusive fiducial volume to take the following values for the VBS cuts

$$m_{jj} > 200 \text{ GeV}, \quad |\Delta y_{jj}| > 2. \quad (11)$$

The figure showing this is Fig. 4, the ratio of double-differential cross sections in the plan $(m_{jj}, \Delta y_{jj})$. Two plots are displayed: the ratio of the $|t|^2 + |u|^2$ and $|s|^2 + |t|^2 + |u|^2$ approximations over the full calculation, respectively. In the first case, the approximation is good within $\pm 10\%$ over the whole range apart in the low invariant-mass region at both low and large rapidity difference. The low rapidity difference region possesses remnants of the tri-bosons contributions. It is therefore expected that the $|t|^2 + |u|^2$ approximation fails in this region. The second plot, where the $|s|^2 + |t|^2 + |u|^2$ approximation is considered, displays a better behaviour in the previously mentioned region. The full calculation is approximated at the level of $\pm 10\%$ everywhere apart in the upper left corner where the inclusion of s -channel contributions did not improve the approximation. This is due to ...

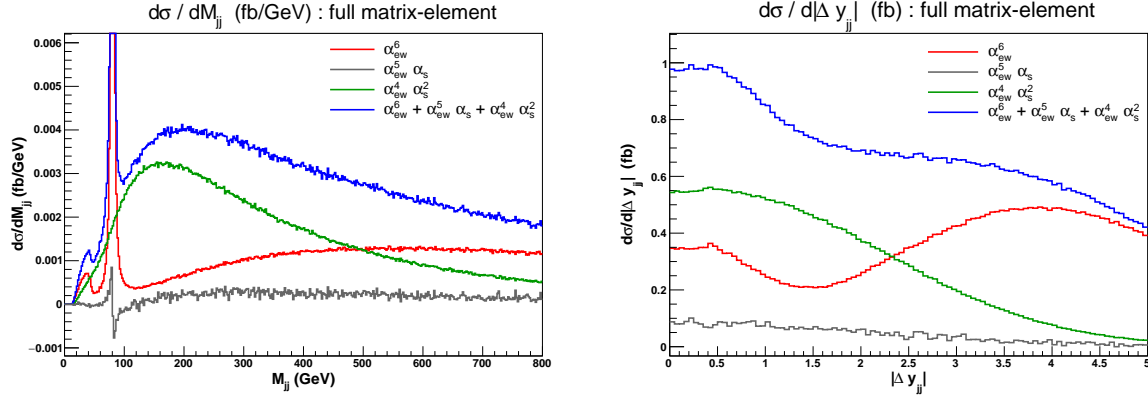


Fig. 2: Differential distribution in the di-jet invariant mass m_{jj} (left) and the difference of the jet rapidities $|\Delta y_{jj}|$ (right) at LO. The EW contribution is in red, the QCD one in green, and the interference in grey. The sum of all the contributions is in blue. No cuts on m_{jj} and $|\Delta y_{jj}|$ are applied. [MP: On the plots: it should be α and not α_{em} and m_{jj} instead of M_{jj} . And we have the convention to put α_s before α .]

4.3 Comparison in the fiducial region

In Tab. 3 we report the total rates at LO accuracy obtained with the set-up described in Eqs. (7-9) with the VBS cuts $m_{jj} > 500$ GeV and $|\Delta y_{jj}| > 2.5$ (see Eq. (10)). The order considered here is the order $\mathcal{O}(\alpha^6)$. We note that several full predictions are not in statistical agreement. These are possibly due to too aggressive estimations of statistical uncertainty or ... [MP: To be added] Nonetheless, all these predictions agree within less than 0.5%. At the level of the cross section, it seems difficult to infer the quality of the the various approximations. This simply means that the various VBS approximations are not worth than 0.5% at the level of the fiducial cross section at LO for a typical phase-space volume used by experimental collaborations.

Code	$\sigma[\text{fb}]$
BONSAY	$X \pm 0.0002$
MG5_AMC	$X \pm 0.001$
MoCANLO+RECOLA	1.4347 ± 0.0001
PHANTOM	1.4374 ± 0.0006
POWHEG	1.44092 ± 0.00009
VBFNLO	1.43796 ± 0.00005
WHIZARD	1.4381 ± 0.0002

Table 3: Cross sections for the LHC process $pp \rightarrow \mu^+ \nu_\mu e^+ \nu_e jj$ at LO accuracy and order $\mathcal{O}(\alpha^6)$. The uncertainties shown refers to the estimated statistical error of the Monte Carlo programs. The predictions are obtained in the fiducial region described in Sec. 3.3. [MP: Please add or check your respective numbers]

In Fig. 5, we show the distributions in the invariant mass (top) and the rapidity difference of the two tag-

ging jets (bottom) which are key observables for VBS measurements. In both cases we show the absolute distributions in the upper plot, while the lower plot displays the ratio over VBFNLO [MP: To be changed to Recola]. For both observables we find a relatively good agreement among the various tools, which confirms the fact that contributions from s -channel diagrams as well as from non-resonant configurations are suppressed in the fiducial region. In general, the agreement is at the level of 1% or below for each bin. We have checked that the same level of agreement holds for other standard differential distributions such as rapidity, invariant mass, transverse momentum. This means that at LO, in the fiducial volume, the VBS approximation is good to a per cent.

5 Next-to-leading order QCD

5.1 Inclusive comparison

We now present the inclusive study performed at NLO QCD for the EW component, namely the order $\mathcal{O}(\alpha_s \alpha^6)$.

According to the results shown in Sec. 4.2, the VBS approximation at LO fails in the region $m_{jj} < 200$ GeV, $|\Delta y_{jj}| < 2$. For the inclusive region (see Eq. (11)), this approximation is good up to $\pm 10\%$ apart for large di-jet differences and low di-jet invariant mass. It is therefore interesting to check how good this approximation is at NLO. Thus, we impose the same kinematic cuts shown in Sec. 3.3 and apply the VBS cuts of Eq. (11).

We compare three different predictions at NLO QCD: BONSAY employs the VBS approximation ($|t|^2 + |u|^2$) while VBFNLO adds the s -channel contributions ($|s|^2 + |t|^2 + |u|^2$). On the other hand RECOLA employs full

matrix elements, adding also t/u interferences, factorisable, and non-factorisable QCD corrections to the order $\mathcal{O}(\alpha^6)$. This means that in order to cancel all IR singularities, also EW correction to the $\mathcal{O}(\alpha_s\alpha^5)$ interference have to be included [15]. The total cross sections within the above mentioned kinematic cuts are shown in Tab. 4.

Prediction	σ_{tot} [fb]	δ
full	1.8120 ± 0.0144	-
$ t ^2 + u ^2$	1.6292 ± 0.0001	-10%
$ s ^2 + t ^2 + u ^2$	1.7780 ± 0.0001	-2%

Table 4: Total cross sections at NLO QCD *i.e.* at order $\mathcal{O}(\alpha_s\alpha^6)$ for the full computation and two approximations. In addition to the cuts of Sec. 3.3, the VBS cuts take the values: $m_{jj} > 200 \text{ GeV}$, $|\Delta y_{jj}| > 2$.

The VBS approximation for NLO QCD predictions (labelled by $|t|^2 + |u|^2$) gives a negative discrepancy of about 10% with respect to the full calculation. The inclusion of s -channel diagrams improves the approximate prediction down to a 2% discrepancy.

These discrepancies are much more evident in differential distributions. In Fig. 6, we show the distributions in the di-jet invariant mass m_{jj} and rapidity separation Δy_{jj} . For large m_{jj} and large Δy_{jj} , as expected, the VBS approximation is performing well and its s -channel extension agree with the full calculation within few per cents. This is in contrast to the region $200 \text{ GeV} < m_{jj} < 500 \text{ GeV}$ and $2 < |\Delta y_{jj}| < 2.5$, the discrepancy between the $|t|^2 + |u|^2$ approximation and the full computation goes up to 30%. The inclusion of s -channels cures partly the discrepancy in these regions. Still, for the very low m_{jj} a small discrepancy of about 5% remains. This might indicate that also interferences (GP: and non-factorizable QCD corrections ? [MP: I don't know, we have to think about it]) are needed in this phase-space region.

In order to investigate further the jet pair kinematics, we divide the $m_{jj}, \Delta y_{jj}$ plane in 2-dimensional bins and analyse the cross sections. In particular we compute in each bin the ratio of the approximated cross sections over the full one. In Fig. 7 and Fig. 8 we show respectively the ratio $\sigma(|t|^2 + |u|^2)/\sigma(\text{full})$ and $\sigma(|s|^2 + |t|^2 + |u|^2)/\sigma(\text{full})$.

As expected, in the low invariant mass-low rapidity separation region of the jet pair the VBS approximation fails badly (up to 40% discrepancies). The inclusion of the s -channel brings down to at most 5%. However, the positive discrepancy shown in the low m_{jj} region (black curve on Fig. 6) can be traced back to the low

m_{jj} , large Δy_{jj} region of Fig. 8. In this region, the two leading jets have soft transverse momenta, according to the following low-angle approximation

$$\begin{aligned} m_{jj}^2 &= 2 p_{T,j_i} p_{T,j_j} (\cosh \Delta y_{j_i j_j} - \cos \Delta \phi_{j_i j_j}) \\ &\approx 2 p_{T,j_i} p_{T,j_j} \cosh \Delta y_{j_i j_j} . \end{aligned} \quad (12)$$

The same positive discrepancy for the $|s|^2 + |t|^2 + |u|^2$ approximation, can be seen in the low p_T region of the leading jet in the left panel of Fig. 9. In the large invariant mass-small rapidity separation region of Fig. 8, discrepancies at the level of 15% are present. This can be traced back to the large p_T and central rapidity region of the leading jets kinematics, shown in Fig. 9. For such distributions, despite the s -channel inclusion, the discrepancy between the approximated and full result is about 5-10 %.

In the VBS signal-region the VBS approximation shows a good agreement with the full calculation as documented in details below.

Concerning leptonic kinematics, we show in Fig. 10 the distributions of the lepton-lepton invariant mass and of the Zeppenfeld variable of the electron [MP: We should defined the Zep var. somewhere]. The VBFNLO result for the $e^+\mu^+$ invariant mass agrees pretty well with the full curve, generated with RECOLA; the BON-SAY curve is about 10 % smaller. The discrepancies are roughly constant over the whole spectrum.

Instead, the right panel of Fig. 10 clearly shows that the Zeppenfeld variable of the positron z_e is strongly affected by the exclusion of s -channels, with increasing discrepancy w.r.t. the full result at large values. The muon variable z_μ behaviour is almost identical to z_e .

In conclusion, both the loose minimum di-jet invariant mass cut and the inclusion of QCD radiative correction make the s -channel contributions less suppressed than at LO, making their inclusion mandatory, in order to provide trustworthy predictions at NLO accuracy. Nevertheless, interferences and non-factorizable QCD corrections should be included to reduce the discrepancies down to the $\approx 1\%$ level, mainly in inclusive analyses. Instead, the VBS approximation at NLO provides a good approximation of full calculations in the kinematic region where VBS contributions are dominant ($M_{jj} \gtrsim 600 \text{ GeV}$, $\Delta y_{jj} \gtrsim 3$), for both total cross section and differential distributions.

5.2 Comparison in the fiducial region

In Tab. 5, the cross sections of the various tools at NLO QCD accuracy are presented. The order considered is

$\mathcal{O}(\alpha_s\alpha^6)$. In contrast with Tab. 3, the NLO predictions seems to visibly differing according to the approximations used already at the level of the fiducial cross section.

Code	$\sigma[\text{fb}]$
BONSAY	$X \pm 0.0009$
MG5_AMC	$X \pm 0.003$
MoCANLO+RECOLA	1.382 ± 0.002
POWHEG	1.3556 ± 0.0009
VBFNLO	1.3916 ± 0.0001

Table 5: Cross sections for the LHC process $pp \rightarrow \mu^+\nu_\mu e^+\nu_e jj$ at NLO accuracy and order $\mathcal{O}(\alpha^6)$. The uncertainties shown refers to estimated statistical error of the Monte Carlo programs. The predictions are obtained in the fiducial region described in Sec. 3.3. [MP: Please add or check your respective numbers.]

The first observation is that the predictions featuring two versions of the VBS approximation (BONSAY and POWHEG) are close. This means that the double-pole approximation on the two W bosons used in BONSAY constitutes a good approximation of the VBS-approximated virtual corrections implemented in POWHEG. Both predictions differ by about 2% with respect to the full computation (MoCANLO+RECOLA). The second observation is that the inclusion of s -channel contributions seems to have a significant impact. Indeed, its inclusion (as done in VBFNLO) approximates the full computation by less than a per-cent (0.7%). This behaviour is most likely due to low di-jet invariant-mass configurations, where s -channel diagrams and interferences are less suppressed than at LO, because of the presence of extra QCD radiation. [MP: To be developed with more physics insight] .

In Figs. (11-13), several differential distributions are shown. All these predictions are performed at NLO accuracy at the order $\mathcal{O}(\alpha_s\alpha^6)$. [MP: Physics and conclusion on interference/non-factorisable etc. effects are not addresses yet in the discussion.]

We start with Fig. 11 which displays the invariant mass (top) and the rapidity separation (bottom) of the two tagging jets. For high invariant mass, all predictions agree rather well. On the other hand, for low invariant mass, the hierarchy present at the level of the cross section is here reproduced. The VBS-approximated predictions (BONSAY and POWHEG) are lower than the full calculation (MoCANLO+RECOLA). The full calculation is rather well approximated by the hybrid VBS approximation implemented in MADGRAPH5_AMC@NLO. Finally, VBFNLO which include as well s -channel contributions provides larger predictions at low invariant

mass. For the rapidity difference between the two tagging jets, the hierarchy between the predictions is rather similar.

Concerning the transverse momentum (top) and rapidity (bottom) of the hardest jet shown in Fig. 12, the situation is rather different. While MADGRAPH5_AMC@NLO is very close to the full prediction for low transverse momentum, it is diverging from it at larger transverse momentum. This is in contrast with BONSAY and POWHEG which approximate the full computation reasonably well over the whole range and in particular the high transverse-momentum region. Finally, VBFNLO predicts higher rates over the whole range apart around 200 GeV where it is in perfect agreement with the complete calculation. Concerning the rapidity of the hardest jet, VBFNLO is in good agreement with MoCANLO+RECOLA in the rapidity range $|y_{j1}| < 3$. For larger rapidity, the other codes constitute a better description of the full process at order $\mathcal{O}(\alpha_s\alpha^6)$.

The last set of differential distributions is the invariant mass of the two charged lepton (top) and the Zeppenfeld variable for the anti-muon (bottom). Concerning the comparison of the predictions, both distributions display a rather similar behaviour. Indeed, the hierarchy mentioned previously is here respected and enhanced towards high invariant mass or high Zeppenfeld variable. MoCANLO+RECOLA and VBFNLO are in rather good agreement for both distributions for the kinematic range displayed here. The other three VBS approximations seem to be close to each other.

6 Matching to parton shower

We now turn to discuss how different predictions compare when the matching to parton-shower (PS) is included. For such a comparison we expect larger discrepancy than what we found at fixed-order, as a consequence of the different matching schemes, PS employed and of the other details of the matching (such as the choice of the shower initial scale). Among the codes capable of providing fixed-order results, presented before, MG5_AMC, POWHEG and VBFNLO can also provide results at (N)LO+PS accuracy. Besides, also PHANTOM is employed for LO+PS results.

MG5_AMC, which employs the MC@NLO [66] matching procedure, will be used together with PYTHIA8 [67] (version 2.2.3) and HERWIG++ [68, 69] (version 2.7.1). For POWHEG, the omonymous matching procedure is employed [70, 48], together with PYTHIA8 **MZ VERSION? if same as MG5, put it at the end together with the tune.** VBFNLO makes it possible to choose between the MC@NLO and POWHEG matching, in both cases together with HERWIG7 CITEREF.

Finally, PHANTOM results will be shown matched with PYTHIA 8 and HERWIG++. Whenever PYTHIA8 is used, the Monash tune [71] is selected.

Results will be presented within the cuts described in Section 3.3, applied after shower and hadronization (this implies that jets are obtained by clustering stable hadrons, and not QCD partons). It follows that at the event-generation level, looser cuts (or no cuts at all) must be employed in order not to bias the results. **MZ lepton-jet separation at the hard-event level?**

A slightly different setup has been employed for MG5_AMC in order to simplify the calculation: instead of generating the full $pp \rightarrow \mu^+ \nu_\mu e^+ \nu_e jj$ process, since it is anyway dominated by doubly-resonant contribution, the events are produced for the process with two stable W^+ bosons ($pp \rightarrow W^+ W^+ jj$), and these W^+ bosons are decayed with MADSPIN [72] (keeping spin correlations) before the PS. Since MADSPIN computes the partial and total decay width of the W bosons at LO accuracy only, while in Section 3.3 the NLO width is employed, a small effect (6%) on the normalisation of distribution is induced. Finally, when the renormalisation and factorisation scales are set, the $\Delta R_{j\ell}$ cut is not imposed during the jet-clustering procedure, but this has no visible effect on the results.

Code	$\sigma[\text{fb}]$
MG5_AMC+PYTHIA8	$1.450(1.368) \pm 0.$
MG5_AMC+HERWIG++	$1.445(1.363) \pm 0.$
POWHEG	1.3633 ± 0.0004
VBFNLO	$1.339 \pm 0.$
MG5_AMC+PYTHIA8 (LO)	$1.352(1.275) \pm 0.$
MG5_AMC+HERWIG++ (LO)	$1.343(1.267) \pm 0.$
PHANTOM+PYTHIA8	$1.235 \pm 0.$
PHANTOM+HERWIG++	$1.260 \pm 0.$

Table 6: Rates at NLO-QCD (LO-QCD) accuracy matched to parton shower within VBS cuts obtained with the different codes used in this comparison, for the $pp \rightarrow \mu^+ \nu_\mu e^+ \nu_e jj$ process. Numbers in parentheses for the MG5_AMC simulations are rescaled to account for the effect related to the boson widths computed by MADSPIN, see the text for details.

MZ: MC uncertainties???

We now turn to present the results of predictions matched to parton shower: the total rates within VBS cuts are displayed in Table 6, both at LO and NLO accuracy. For MG5_AMC, the numbers in parentheses are rescaled to take into account the width effects described in the above paragraph. Once this effect is taken into account, total rates from different tools agree

within few percents. Larger discrepancies however will appear for differential observables, which we are going to discuss in the following. For any observable, results will be presented in two plots, shown side-by-side. In the plot on the left (right), (N)LO+PS predictions are shown with different colours in the main frame. In the inset, these predictions are compared in both cases with the fixed-order prediction at NLO accuracy (obtained with VBFNLO). For the differential observables, the MG5_AMC predictions are *not* rescaled to compensate for the width effect mentioned above.

The first observable we investigate is the exclusive jet multiplicity, shown in Figure 14. Looking at the LO+PS predictions, one can appreciate that the main effects are driven by the parton shower that is employed HERWIG++/7 or PYTHIA8, with the clear tendency of producing more radiation for the latter, leading to higher jet multiplicities. Difference among tools that employ the same parton shower are typically smaller, and can be traced back to different values of the initial scale of the shower. The main effect of NLO corrections for this (rather inclusive) observable is to stabilize the predictions for the two-jet bin, where discrepancies among tools are reduced to about 10%. For the three-jet bin, which is described only at LO accuracy, differences among tools remain large: the largest rate is predicted by MG5_AMC, while the smallest rate is predicted by POWHEG, both matched to PYTHIA8. Despite the fact that the same parton shower is employed, the way emissions are treated is different among the two tools. In particular, for POWHEG, the first emission is generated with an internal Sudakov form factor (the prediction dubbed POWHEG-NO SHOWER corresponds to stopping after the first emission), while for MG5_AMC there is an interplay between the real-emission matrix element and the shower emission.

The next observable that we study is the invariant mass of the two tagging jets, shown in Figure 15. For this observable, both at LO+PS and NLO+PS, the spread of predictions matched with parton shower is rather small ($\lesssim 10\%$, if one compensates for the 6% width effect for MG5_AMC); LO+PS predictions tend to be significantly softer than the fixed NLO one, with an effect of about -30% at the end of the displayed range. At NLO+PS, this effect is much mitigated, owing to the better description of the first QCD emission which is now driven by the real-emission matrix element.

The rapidity difference between the two tagging jets, shown in Figure 16 has some similarities to the invariant-mass distribution: at LO+PS all predictions, except for VBFNLO3+HERWIG7 where the effect is mitigated, show the tendency to deplete the large-separation re-

gion with respect to the fixed-order prediction, in a quantitatively similar way. At NLO+PS, when the extra radiation is described by the real matrix element, such an effect is greatly reduced. A notable exception is the POWHEG prediction, which still shows a suppression at large separations: since such a suppression is already there for the POWHEG-NO SHOWER sample, it is very likely that it is driven by the way the first emission is generated. A minor effect in the same direction is visible in the last two bins of the MG5_AMC+HERWIG++ prediction (although with rather large statistical uncertainties).

The transverse momentum of the hardest and second-hardest jets are shown in Figures 17 and 18 respectively. In general, for both observables, predictions from different tools agree rather well with each other, with a spread at most at the 10% level. At LO+PS, typically the transvers-momentum spectra are softer than the fixed-NLO one, and this effect is more marked for the second-hardest jet which, as expected, is more sensitive to the description of the extra radiation. Again, this effect is mitigated by NLO corrections. The only feature that it may be worth to notice among the NLO+PS predictions is the tendency of POWHEG to suppress the hardest-jet spectrum at low transverse momentum ($p_T < 100$ GeV).

If we consider the rapidity of the second jet, Figure 19, we observe again rather small differences among tools, with the tendency towards a general stabilization at NLO+PS. However, some (small) differences in the shape remain at NLO+PS, which are worth to be briefly discussed: predictions obtained with MG5_AMC are very close to the fixed-order prediction; POWHEG displays an enhancement of the central region, and a consequent suppression in the peripheral region, while VBFNLO shows an opposite behaviour. However, the effect is rather small, with the largest departure from the fixed-order prediction being at most 10%.

Finally, focusing on the third jet, we conclude the list of differential observables with the rapidity and the z variable, Figures 20 and 21. **MZ the rapidity can be dropped (check also the following discussion in case); if z is defined elsewhere in the paper, then add a ref to the proper section. Otherwise define it here** In general, for observables which involve the third jet, one can clearly see a degradation of the agreement among the various tools, because of the poorer perturbative description of these observables. The rapidity and z variable are a striking example: both at LO and NLO, the tendency of PYTHIA8 to generate more hard and central radiation (corresponding to low values of z) is clearly visible; it is interesting to notice that this effect survives beyond

the first emission, as it can be observed by comparing POWHEG-NO SHOWER with POWHEG+PYTHIA8. If it is true that the central enhancement is a bit mitigated if NLO+PS tools are used (compare LO+PS and NLO+PS from MG5_AMC+PYTHIA8 with the fixed-NLO prediction), however even at NLO+PS the central region ($z_{j3} < 0.5$) is cursed by huge differences between tools. Large differences, reaching a factor 2, persist also away from the central region.

In conclusion, the comparison of tools including matching with parton-shower clearly shows the benefits of the inclusion of NLO corrections: for most observables described effectively at NLO accuracy differences between tools are at (or below) the 10% level. **MZ compare this number with scale uncertainties** Some exceptions exist, e.g. the rapidity separation of the two tagging jets, which on the one hand clearly suggest not to rely on a single tool/parton shower, and on the other make it worth to investigate more in details the way QCD radiation is generated **MZ cite here H VBF at NNLO?**. Finally, the size of discrepancies for observables that are described at a lower perturbative accuracy, notably those related to the third jet, suggest that experimental analyses should rely as least as possible on those observables and, in any case, use conservative estimate of the theory uncertainties. In order to improve the description of these observables, a simulation of VBS+j at NLO, currently unavailable but within the reach of modern automated tools, is certainly desirable.

7 Conclusion

- Sum-up of the study.

[MP: This might deserve a section on its own.]

Recommendations to experimental collaborations:

- Combinations with EW NLO corrections.
- Missing higher EW order: $\pm\delta_{\text{NLOEW}}^2$
- Systematics when using NLO QCD approximation
- Systematics of different parton shower
- Combined measurement including EW, QCD, and interference
- Move to NLO predictions / generators
- Comment on the irreducible QCD background
- Uncertainties related to PDF. Some of us have already presented preliminary results on this subject []. A forthcoming article will addresses related questions.

Acknowledgements

The authors would like to acknowledge the contribution of the COST Action CA16108 which initiated this work. Moreover, this work was supported by a STSM Grant from COST Action CA16108.

BB, AD, and MP acknowledges financial support by the German Federal Ministry for Education and Research (BMBF) under contract no. 05H15WWCA1 and the German Science Foundation (DFG) under reference number DE 623/6-1.

Appendix A: Appendix one

References

1. **ATLAS** Collaboration, G. Aad *et al.*, *Evidence for Electroweak Production of $W^\pm W^\pm jj$ in pp Collisions at $\sqrt{s} = 8$ TeV with the ATLAS Detector*. Phys. Rev. Lett. **113** (2014) no. 14, 141803, [arXiv:1405.6241 \[hep-ex\]](#).
2. **CMS** Collaboration, V. Khachatryan *et al.*, *Study of vector boson scattering and search for new physics in events with two same-sign leptons and two jets*. Phys. Rev. Lett. **114** (2015) no. 5, 051801, [arXiv:1410.6315 \[hep-ex\]](#).
3. **CMS** Collaboration, A. M. Sirunyan *et al.*, *Observation of electroweak production of same-sign W boson pairs in the two jet and two same-sign lepton final state in proton-proton collisions at $\sqrt{s} = 13$ TeV*. [arXiv:1709.05822 \[hep-ex\]](#).
4. **ATLAS** Collaboration, M. Aaboud *et al.*, *Measurement of $W^\pm W^\pm$ vector-boson scattering and limits on anomalous quartic gauge couplings with the ATLAS detector*. Phys. Rev. **D96** (2017) 012007, [arXiv:1611.02428 \[hep-ex\]](#).
5. B. Jäger, C. Oleari, and D. Zeppenfeld, *Next-to-leading order QCD corrections to W^+W^+jj and W^-W^-jj production via weak-boson fusion*. Phys. Rev. **D80** (2009) 034022, [arXiv:0907.0580 \[hep-ph\]](#).
6. B. Jäger and G. Zanderighi, *NLO corrections to electroweak and QCD production of W^+W^+ plus two jets in the POWHEGBOX*. JHEP **11** (2011) 055, [arXiv:1108.0864 \[hep-ph\]](#).
7. A. Denner, L. Hošeková, and S. Kallweit, *NLO QCD corrections to W^+W^+jj production in vector-boson fusion at the LHC*. Phys. Rev. **D86** (2012) 114014, [arXiv:1209.2389 \[hep-ph\]](#).
8. M. Rauch, *Vector-Boson Fusion and Vector-Boson Scattering*. [arXiv:1610.08420 \[hep-ph\]](#).
9. T. Melia, K. Melnikov, R. Röntsch, and G. Zanderighi, *Next-to-leading order QCD predictions for W^+W^+jj production at the LHC*. JHEP **12** (2010) 053, [arXiv:1007.5313 \[hep-ph\]](#).
10. T. Melia, P. Nason, R. Röntsch, and G. Zanderighi, *W^+W^+ plus dijet production in the POWHEGBOX*. Eur. Phys. J. **C71** (2011) 1670, [arXiv:1102.4846 \[hep-ph\]](#).
11. F. Campanario, M. Kerner, L. D. Ninh, and D. Zeppenfeld, *Next-to-leading order QCD corrections to W^+W^+ and W^-W^- production in association with two jets*. Phys. Rev. **D89** (2014) no. 5, 054009, [arXiv:1311.6738 \[hep-ph\]](#).
12. J. Baglio *et al.*, *Release Note - VBFNLO 2.7.0*. [arXiv:1404.3940 \[hep-ph\]](#).
13. B. Biedermann, A. Denner, and M. Pellen, *Complete NLO corrections to W^+W^+ scattering and its irreducible background at the LHC*. JHEP **10** (2017) 124, [arXiv:1708.00268 \[hep-ph\]](#).
14. C. F. Anders *et al.*, “VBScan Split 2017 Workshop Summary,” 2018. [arXiv:1801.04203 \[hep-ph\]](#).
15. B. Biedermann, A. Denner, and M. Pellen, *Large electroweak corrections to vector-boson scattering at the Large Hadron Collider*. Phys. Rev. Lett. **118** (2017) no. 26, 261801, [arXiv:1611.02951 \[hep-ph\]](#).
16. I. Kuss and H. Spiesberger, *Luminosities for vector boson - vector boson scattering at high-energy colliders*. Phys. Rev. **D53** (1996) 6078–6093, [arXiv:hep-ph/9507204 \[hep-ph\]](#).
17. E. Accomando, A. Denner, and S. Pozzorini, *Logarithmic electroweak corrections to $e^+e^- \rightarrow \nu_e \bar{\nu}_e W^+W^-$* . JHEP **03** (2007) 078, [arXiv:hep-ph/0611289 \[hep-ph\]](#).
18. S. Dawson, *The Effective W Approximation*. Nucl. Phys. **B249** (1985) 42–60.
19. M. J. Duncan, G. L. Kane, and W. W. Repko, *W Physics at Future Colliders*. Nucl. Phys. **B272** (1986) 517–559.
20. R. N. Cahn and S. Dawson, *Production of Very Massive Higgs Bosons*. Phys. Lett. **136B** (1984) 196. [Erratum: Phys. Lett.138B,464(1984)].
21. S. Dittmaier and C. Schwan, *Non-factorizable photonic corrections to resonant production and decay of many unstable particles*. Eur. Phys. J. **C76** (2016) no. 3, 144, [arXiv:1511.01698 \[hep-ph\]](#).
22. S. Dittmaier and M. Roth, *LUSIFER: A LUCid approach to six FERMion production*. Nucl. Phys. **B642** (2002) 307–343, [arXiv:hep-ph/0206070 \[hep-ph\]](#).

23. A. Denner, S. Dittmaier, and L. Hofer, *COLLIER - A fortran-library for one-loop integrals*. PoS **LL2014** (2014) 071, [arXiv:1407.0087 \[hep-ph\]](#).
24. A. Denner, S. Dittmaier, and L. Hofer, *COLLIER: a fortran-based Complex One-Loop Library in Extended Regularizations*. Comput. Phys. Commun. **212** (2017) 220–238, [arXiv:1604.06792 \[hep-ph\]](#).
25. J. Alwall *et al.*, *The automated computation of tree-level and next-to-leading order differential cross sections, and their matching to parton shower simulations*. JHEP **07** (2014) 079, [arXiv:1405.0301 \[hep-ph\]](#).
26. S. Frixione, Z. Kunszt, and A. Signer, *Three jet cross-sections to next-to-leading order*. Nucl. Phys. **B467** (1996) 399–442, [arXiv:hep-ph/9512328 \[hep-ph\]](#).
27. S. Frixione, *A General approach to jet cross-sections in QCD*. Nucl. Phys. **B507** (1997) 295–314, [arXiv:hep-ph/9706545 \[hep-ph\]](#).
28. R. Frederix, S. Frixione, F. Maltoni, and T. Stelzer, *Automation of next-to-leading order computations in QCD: The FKS subtraction*. JHEP **10** (2009) 003, [arXiv:0908.4272 \[hep-ph\]](#).
29. R. Frederix, S. Frixione, A. S. Papanastasiou, S. Prestel, and P. Torrielli, *Off-shell single-top production at NLO matched to parton showers*. JHEP **06** (2016) 027, [arXiv:1603.01178 \[hep-ph\]](#).
30. G. Ossola, C. G. Papadopoulos, and R. Pittau, *Reducing full one-loop amplitudes to scalar integrals at the integrand level*. Nucl. Phys. **B763** (2007) 147–169, [arXiv:hep-ph/0609007 \[hep-ph\]](#).
31. P. Mastrolia, E. Mirabella, and T. Peraro, *Integrand reduction of one-loop scattering amplitudes through Laurent series expansion*. JHEP **06** (2012) 095, [arXiv:1203.0291 \[hep-ph\]](#). [Erratum: JHEP11,128(2012)].
32. G. Passarino and M. J. G. Veltman, *One-loop corrections for e^+e^- annihilation into $\mu^+\mu^-$ in the Weinberg model*. Nucl. Phys. **B160** (1979) 151–207.
33. A. I. Davydychev, *A Simple formula for reducing Feynman diagrams to scalar integrals*. Phys. Lett. **B263** (1991) 107–111.
34. A. Denner and S. Dittmaier, *Reduction schemes for one-loop tensor integrals*. Nucl. Phys. **B734** (2006) 62–115, [hep-ph/0509141](#).
35. V. Hirschi, R. Frederix, S. Frixione, M. V. Garzelli, F. Maltoni, and R. Pittau, *Automation of one-loop QCD corrections*. JHEP **05** (2011) 044, [arXiv:1103.0621 \[hep-ph\]](#).
36. G. Ossola, C. G. Papadopoulos, and R. Pittau, *CutTools: A Program implementing the OPP reduction method to compute one-loop amplitudes*. JHEP **03** (2008) 042, [arXiv:0711.3596 \[hep-ph\]](#).
37. T. Peraro, *Ninja: Automated Integrand Reduction via Laurent Expansion for One-Loop Amplitudes*. Comput. Phys. Commun. **185** (2014) 2771–2797, [arXiv:1403.1229 \[hep-ph\]](#).
38. V. Hirschi and T. Peraro, *Tensor integrand reduction via Laurent expansion*. JHEP **06** (2016) 060, [arXiv:1604.01363 \[hep-ph\]](#).
39. H.-S. Shao, *Iregi user manual, unpublished*.
40. F. Cascioli, P. Maierhöfer, and S. Pozzorini, *Scattering Amplitudes with Open Loops*. Phys. Rev. Lett. **108** (2012) 111601, [arXiv:1111.5206 \[hep-ph\]](#).
41. A. Ballestrero, A. Belhouari, G. Bevilacqua, V. Kashkan, and E. Maina, *PHANTOM: A Monte Carlo event generator for six parton final states at high energy colliders*. Comput. Phys. Commun. **180** (2009) 401–417, [arXiv:0801.3359 \[hep-ph\]](#).
42. A. Denner and S. Dittmaier, *The Complex-mass scheme for perturbative calculations with unstable particles*. Nucl. Phys. Proc. Suppl. **160** (2006) 22–26, [arXiv:hep-ph/0605312 \[hep-ph\]](#). [22(2006)].
43. A. Ballestrero, “PHACT: Helicity amplitudes for present and future colliders,” in *High energy physics and quantum field theory. Proceedings, 14th International Workshop, QFTHEP’99, Moscow, Russia, May 27-June 2, 1999*, pp. 303–309. 1999. [arXiv:hep-ph/9911318 \[hep-ph\]](#).
44. A. Ballestrero and E. Maina, *A New method for helicity calculations*. Phys. Lett. **B350** (1995) 225–233, [arXiv:hep-ph/9403244 \[hep-ph\]](#).
45. F. A. Berends, P. H. Daverveldt, and R. Kleiss, *Complete Lowest Order Calculations for Four Lepton Final States in electron-Positron Collisions*. Nucl. Phys. **B253** (1985) 441–463.
46. G. P. Lepage, *A New Algorithm for Adaptive Multidimensional Integration*. J. Comput. Phys. **27** (1978) 192.
47. S. Alioli, P. Nason, C. Oleari, and E. Re, *A general framework for implementing NLO calculations in shower Monte Carlo programs: the POWHEG BOX*. JHEP **06** (2010) 043, [arXiv:1002.2581 \[hep-ph\]](#).
48. S. Frixione, P. Nason, and C. Oleari, *Matching NLO QCD computations with Parton Shower simulations: the POWHEG method*. JHEP **11**

- (2007) 070, [arXiv:0709.2092 \[hep-ph\]](#).
49. K. Arnold *et al.*, *VBFNLO: A Parton level Monte Carlo for processes with electroweak bosons*. Comput. Phys. Commun. **180** (2009) 1661–1670, [arXiv:0811.4559 \[hep-ph\]](#).
 50. K. Arnold *et al.*, *VBFNLO: A Parton Level Monte Carlo for Processes with Electroweak Bosons – Manual for Version 2.5.0*. [arXiv:1107.4038 \[hep-ph\]](#).
 51. S. Actis *et al.*, *Recursive generation of one-loop amplitudes in the Standard Model*. JHEP **04** (2013) 037, [arXiv:1211.6316 \[hep-ph\]](#).
 52. S. Actis *et al.*, *RECOLA: REcursive Computation of One-Loop Amplitudes*. Comput. Phys. Commun. **214** (2017) 140–173, [arXiv:1605.01090 \[hep-ph\]](#).
 53. F. A. Berends, R. Pittau, and R. Kleiss, *All electroweak four fermion processes in electron - positron collisions*. Nucl. Phys. **B424** (1994) 308–342, [arXiv:hep-ph/9404313 \[hep-ph\]](#).
 54. A. Denner *et al.*, *Predictions for all processes $e^+e^- \rightarrow 4 \text{ fermions} + \gamma$* . Nucl. Phys. **B560** (1999) 33–65, [arXiv:hep-ph/9904472](#).
 55. S. Catani and M. H. Seymour, *A general algorithm for calculating jet cross-sections in NLO QCD*. Nucl. Phys. **B485** (1997) 291–419, [arXiv:hep-ph/9605323 \[hep-ph\]](#). [Erratum: Nucl. Phys. **B510** (1998) 503].
 56. S. Dittmaier, *A general approach to photon radiation off fermions*. Nucl. Phys. **B565** (2000) 69–122, [arXiv:hep-ph/9904440](#).
 57. M. Moretti, T. Ohl, and J. Reuter, *O'Mega: An Optimizing matrix element generator*. [arXiv:hep-ph/0102195 \[hep-ph\]](#).
 58. W. Kilian, T. Ohl, and J. Reuter, *WHIZARD: Simulating Multi-Particle Processes at LHC and ILC*. Eur. Phys. J. **C71** (2011) 1742, [arXiv:0708.4233 \[hep-ph\]](#).
 59. NNPDF Collaboration, R. D. Ball *et al.*, *Parton distributions for the LHC Run II*. JHEP **04** (2015) 040, [arXiv:1410.8849 \[hep-ph\]](#).
 60. A. Buckley, J. Ferrando, S. Lloyd, K. Nordström, B. Page, M. Rüfenacht, M. Schönherr, and G. Watt, *LHAPDF6: parton density access in the LHC precision era*. Eur. Phys. J. **C75** (2015) 132, [arXiv:1412.7420 \[hep-ph\]](#).
 61. D. Yu. Bardin, A. Leike, T. Riemann, and M. Sachwitz, *Energy-dependent width effects in e^+e^- -annihilation near the Z-boson pole*. Phys. Lett. **B206** (1988) 539–542.
 62. A. Denner, S. Dittmaier, M. Roth, and D. Wackeroth, *Electroweak radiative corrections to $e^+e^- \rightarrow WW \rightarrow 4 \text{ fermions}$ in double-pole approximation: The RACOONWW approach*. Nucl. Phys. **B587** (2000) 67–117, [arXiv:hep-ph/0006307 \[hep-ph\]](#).
 63. A. Denner *et al.*, *Electroweak corrections to charged-current $e^+e^- \rightarrow 4 \text{ fermion}$ processes: Technical details and further results*. Nucl. Phys. **B724** (2005) 247–294, [arXiv:hep-ph/0505042](#).
 64. CMS Collaboration, *Observation of electroweak production of same-sign W boson pairs in the two jet and two same-sign lepton final state in proton-proton collisions at 13 TeV*. CMS-PAS-SMP-17-004.
 65. M. Cacciari, G. P. Salam, and G. Soyez, *The anti- k_t jet clustering algorithm*. JHEP **04** (2008) 063, [arXiv:0802.1189 \[hep-ph\]](#).
 66. S. Frixione and B. R. Webber, *Matching NLO QCD computations and parton shower simulations*. JHEP **06** (2002) 029, [arXiv:hep-ph/0204244 \[hep-ph\]](#).
 67. T. Sjöstrand, S. Ask, J. R. Christiansen, R. Corke, N. Desai, P. Ilten, S. Mrenna, S. Prestel, C. O. Rasmussen, and P. Z. Skands, *An Introduction to PYTHIA 8.2*. Comput. Phys. Commun. **191** (2015) 159–177, [arXiv:1410.3012 \[hep-ph\]](#).
 68. M. Bahr *et al.*, *Herwig++ Physics and Manual*. Eur. Phys. J. **C58** (2008) 639–707, [arXiv:0803.0883 \[hep-ph\]](#).
 69. J. Bellm *et al.*, *Herwig++ 2.7 Release Note*. [arXiv:1310.6877 \[hep-ph\]](#).
 70. P. Nason, *A New method for combining NLO QCD with shower Monte Carlo algorithms*. JHEP **11** (2004) 040, [arXiv:hep-ph/0409146 \[hep-ph\]](#).
 71. P. Skands, S. Carrazza, and J. Rojo, *Tuning PYTHIA 8.1: the Monash 2013 Tune*. Eur. Phys. J. **C74** (2014) no. 8, 3024, [arXiv:1404.5630 \[hep-ph\]](#).
 72. P. Artoisenet, R. Frederix, O. Mattelaer, and R. Rietkerk, *Automatic spin-entangled decays of heavy resonances in Monte Carlo simulations*. JHEP **03** (2013) 015, [arXiv:1212.3460 \[hep-ph\]](#).

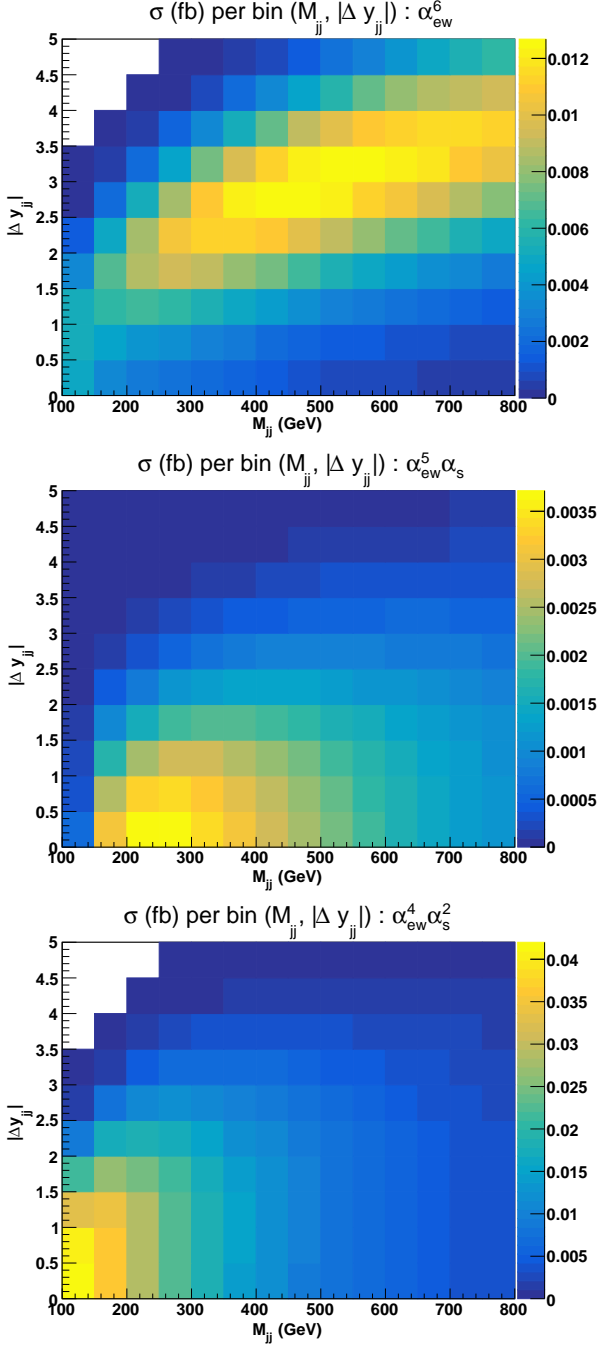


Fig. 3: Cross sections (fb) per bin in the plan $(m_{jj}, \Delta y_{jj})$ for the three LO contributions of orders $\mathcal{O}(\alpha^6)$ (top), $\mathcal{O}(\alpha_s \alpha^5)$ (middle), and $\mathcal{O}(\alpha_s^2 \alpha^4)$ (bottom). [MP: On the plots: it should be α and not α_{em} and m_{jj} instead of M_{jj} . And we have the convention to put α_s before α .]

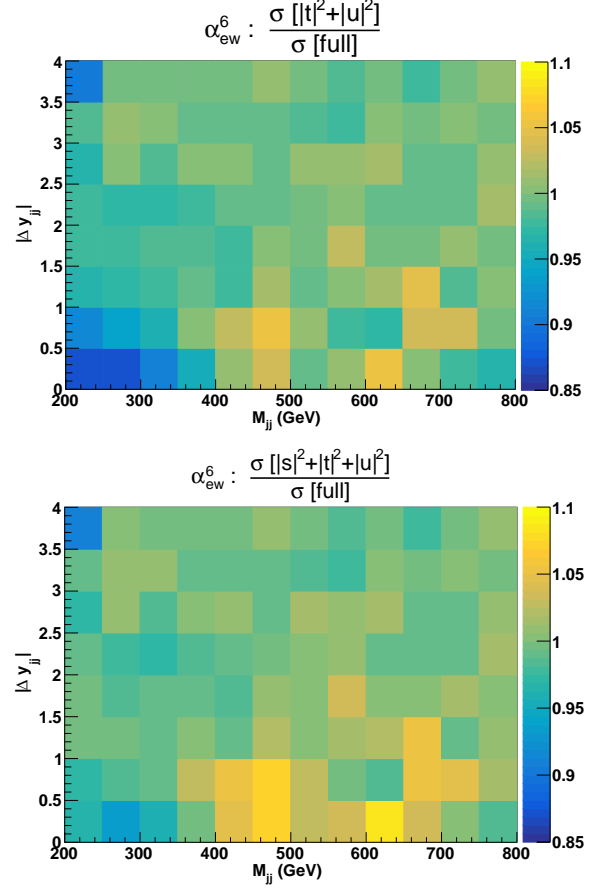


Fig. 4: Cross sections (fb) per bin in the plan $(m_{jj}, \Delta y_{jj})$ at order $\mathcal{O}(\alpha^6)$. Ratio of approximated squared amplitudes over the full matrix element. The approximated squared amplitudes are computed as $|\mathcal{A}|^2 \sim |t|^2 + |u|^2$ (top) and $|\mathcal{A}|^2 \sim |s|^2 + |t|^2 + |u|^2$ (bottom).

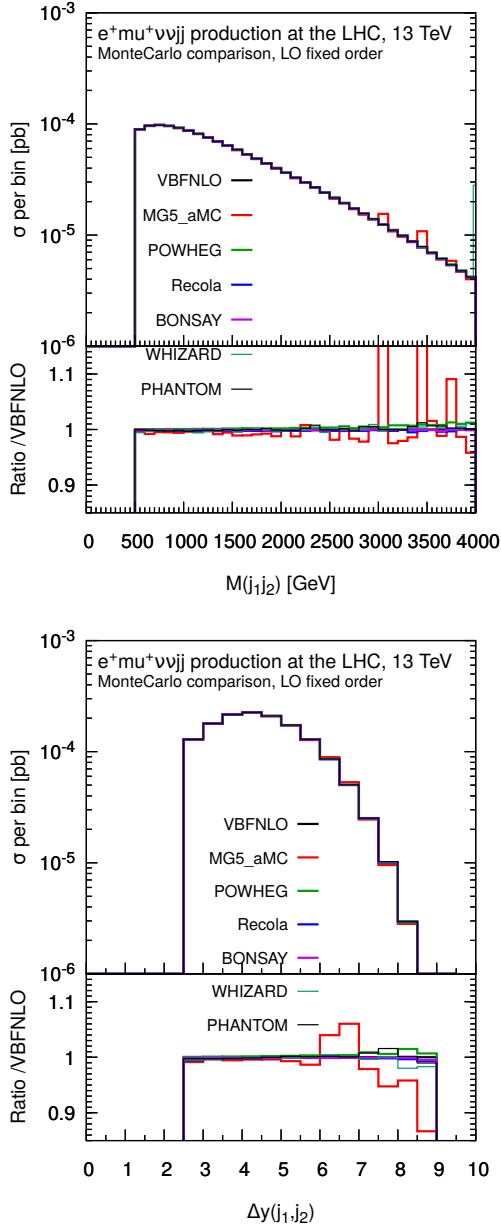


Fig. 5: Differential distributions in the invariant mass (top) and rapidity difference of the two tagging jets (bottom). The LHC process considered is $pp \rightarrow \mu^+\nu_\mu e^+\nu_e jj$ at LO accuracy and order $\mathcal{O}(\alpha^6)$. The description of the different programs used can be found in Sec. 3.2. The upper plots provides the absolute value for each prediction while the lower plots presents all predictions normalised to MoCANLO+RECOLA which is one of the full predictions. The predictions are obtained in the fiducial region described in Sec. 3.3. [MP: MG statistics should be improved and the baseline changed to Recola.]

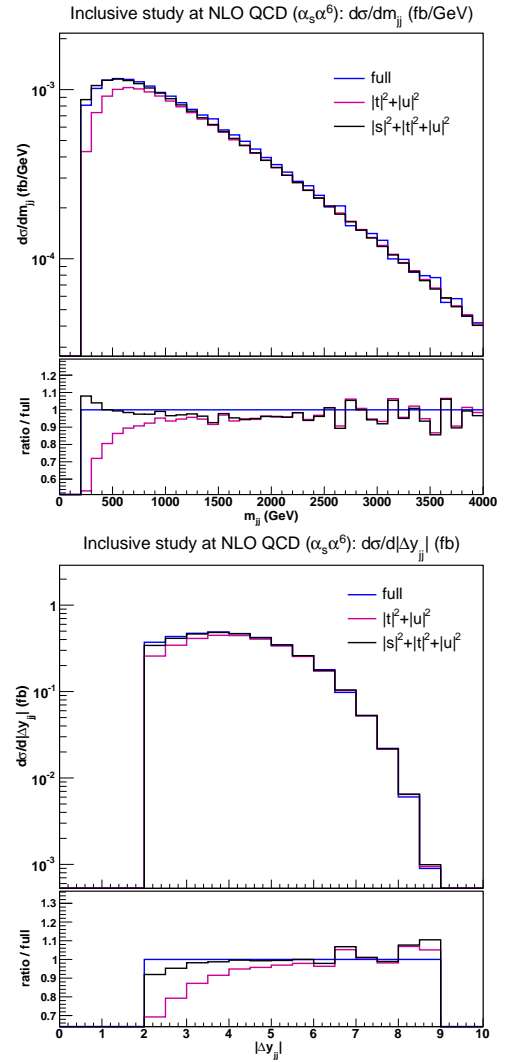


Fig. 6: NLO QCD inclusive study: distributions in m_{jj} (left) and Δy_{jj} (right), obtained with full (RECOLA) and approximated (VBFNLO, BONSAY) amplitudes at order $\mathcal{O}(\alpha_s\alpha^6)$.

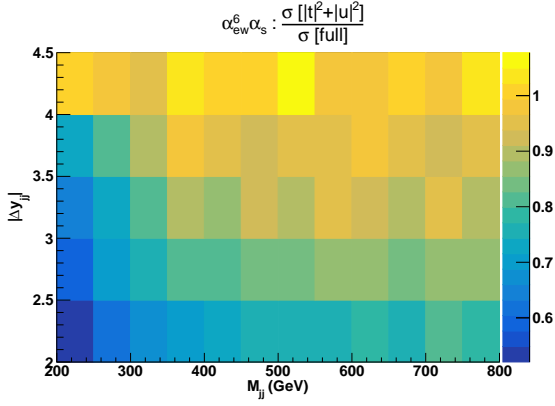


Fig. 7: Cross sections (fb) per bin of $(m_{jj}, \Delta y_{jj})$ at NLO QCD $\mathcal{O}(\alpha_s \alpha^6)$, without any cut on the jj pair kinematics: ratio of approximated squared amplitudes over the full matrix element. The approximated squared amplitudes are computed as $|\mathcal{A}|^2 \sim |t|^2 + |u|^2$. Results of BONSAY (approximated) and RECOLA (full) calculations. **GP: notation to be changed, $M_{jj} > m_{jj}$, alphas alpha**

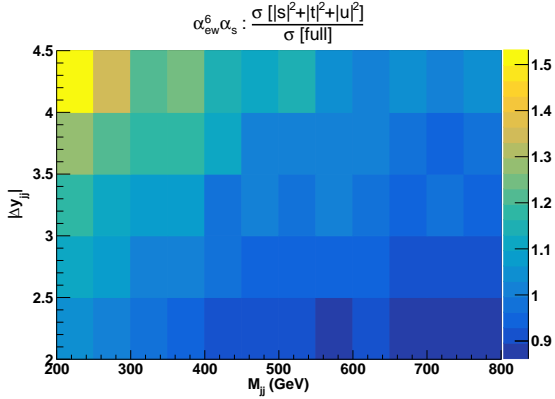


Fig. 8: Cross section (fb) per bin of $(m_{jj}, \Delta y_{jj})$ at NLO QCD $\mathcal{O}(\alpha_s \alpha^6)$, without any cut on the jj pair kinematics: ratio of approximated squared amplitudes over the full matrix element. The approximated squared amplitudes are computed as $|\mathcal{A}|^2 \sim |s|^2 + |t|^2 + |u|^2$. Results of VBFNLO (approximated) and RECOLA (full) calculations. **GP: notation to be changed, $M_{jj} > m_{jj}$, alphas alpha**

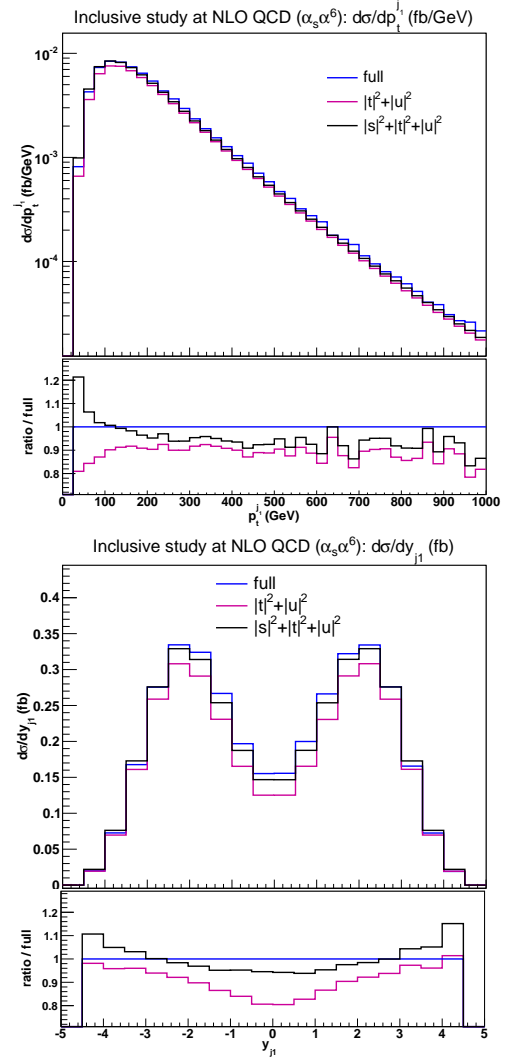


Fig. 9: NLO QCD inclusive study: transverse momentum and rapidity distributions of the leading jet, obtained with full (RECOLA) and approximated (VBFNLO, BONSAY) amplitudes at order $\mathcal{O}(\alpha_s \alpha^6)$.

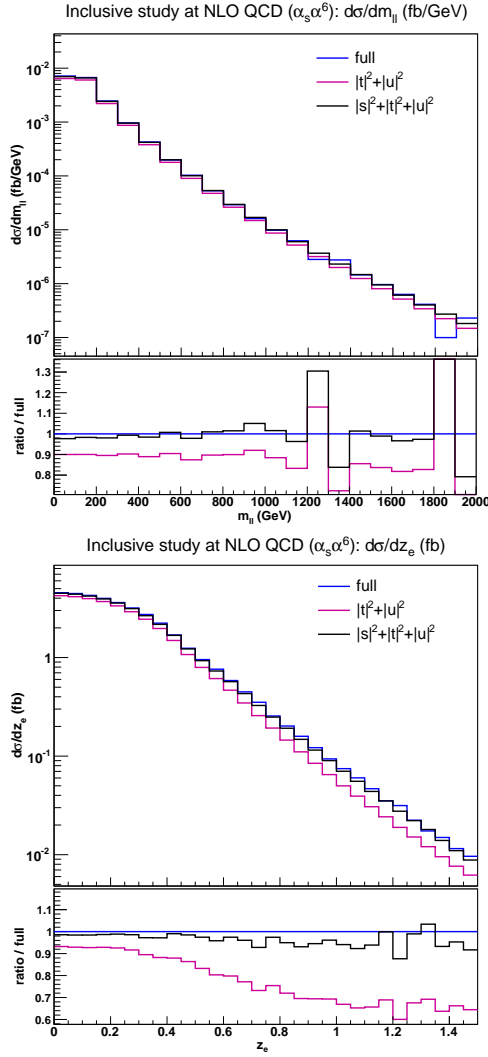


Fig. 10: NLO QCD inclusive study: distributions of the lepton–lepton invariant mass and the electron Zepfenfeld variable, obtained with full (RECOLA) and approximated (VBFNLO, BONSAY) amplitudes at order $\mathcal{O}(\alpha_s\alpha^6)$.

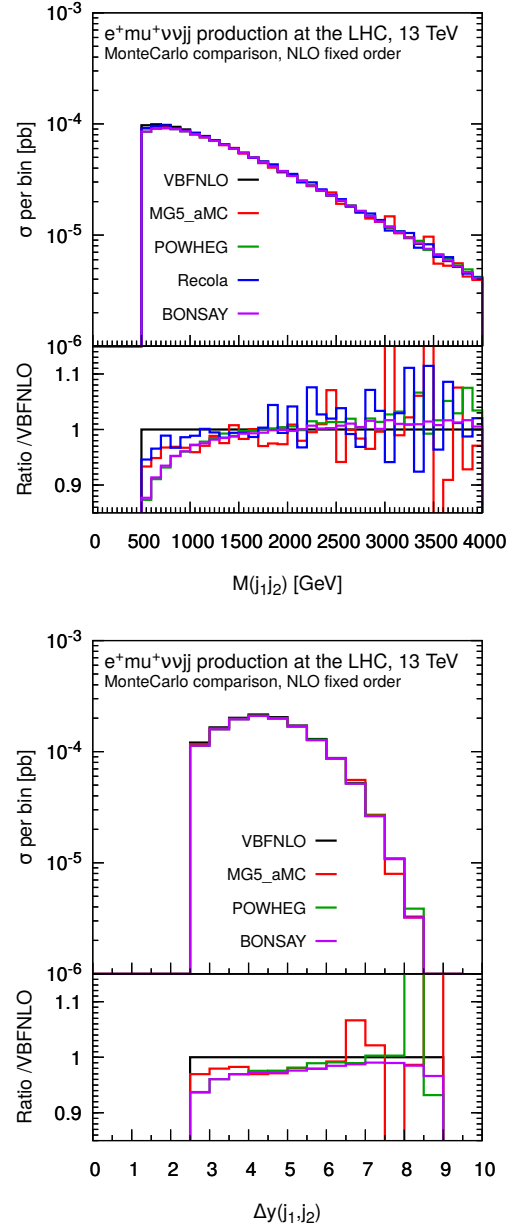


Fig. 11: Differential distributions in the invariant mass (top) and rapidity difference of the two tagging jets (bottom). The LHC process considered is $pp \rightarrow \mu^+\nu_\mu e^+\nu_e jj$ at NLO accuracy and order $\mathcal{O}(\alpha_s\alpha^6)$. The description of the different programs used can be found in Sec. 3.2. The upper plots provides the absolute value for each prediction while the lower plots presents all predictions normalised to MoCANLO+RECOLA which is one of the full predictions. The predictions are obtained in the fiducial region described in Sec. 3.3. [MP: MG statistics should be improved and the baseline changed to Recola.]

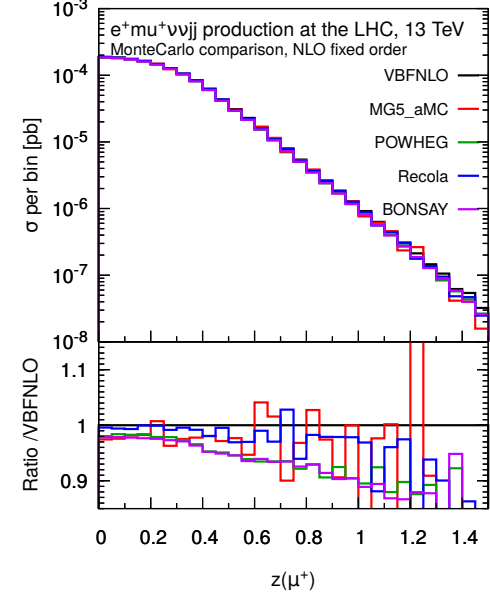
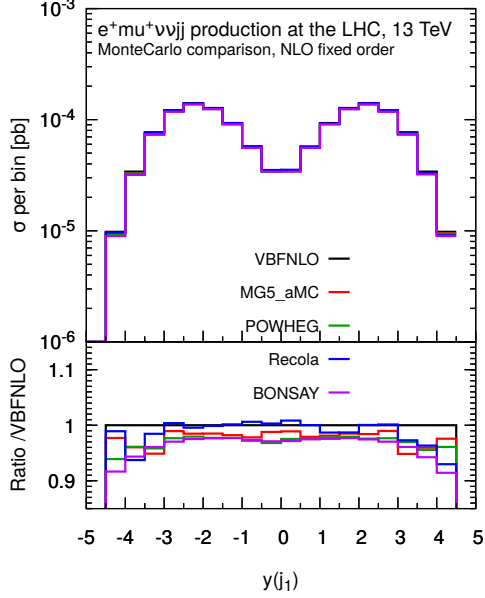
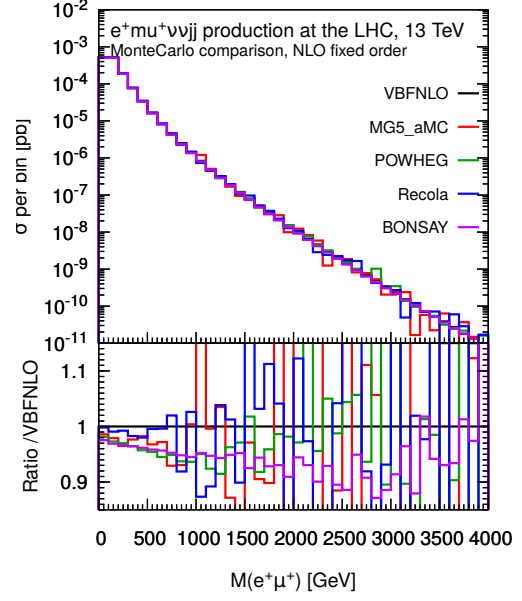
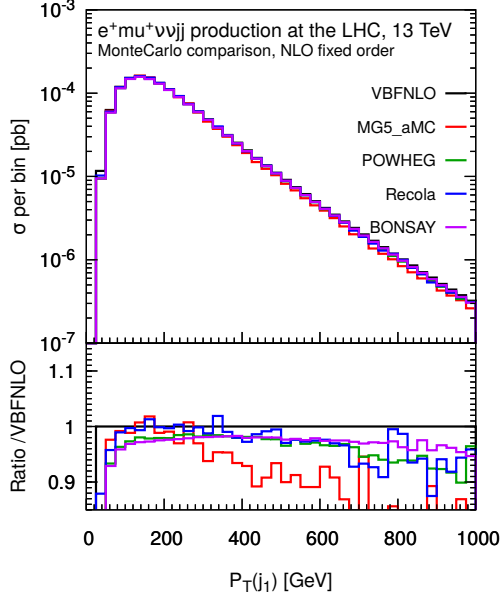


Fig. 12: Differential distributions in the transverse momentum (top) and rapidity of the hardest jet (bottom). The LHC process considered is $pp \rightarrow \mu^+ \nu_\mu e^+ \nu_e jj$ at NLO accuracy and order $\mathcal{O}(\alpha_s \alpha^6)$. The description of the different programs used can be found in Sec. 3.2. The upper plots provides the absolute value for each prediction while the lower plots presents all predictions normalised to MoCANLO+RECOLA which is one of the full predictions. The predictions are obtained in the fiducial region described in Sec. 3.3. [MP: MG statistics should be improved and the baseline changed to Recola.]

Fig. 13: Differential distributions in the invariant mass of the two charged leptons (top) and Zeppenfeld variable for the muon (bottom). The LHC process considered is $pp \rightarrow \mu^+ \nu_\mu e^+ \nu_e jj$ at NLO accuracy and order $\mathcal{O}(\alpha_s \alpha^6)$. The description of the different programs used can be found in Sec. 3.2. The upper plots provides the absolute value for each prediction while the lower plots presents all predictions normalised to MoCANLO+RECOLA which is one of the full predictions. The predictions are obtained in the fiducial region described in Sec. 3.3. [MP: MG statistics should be improved and the baseline changed to Recola.]

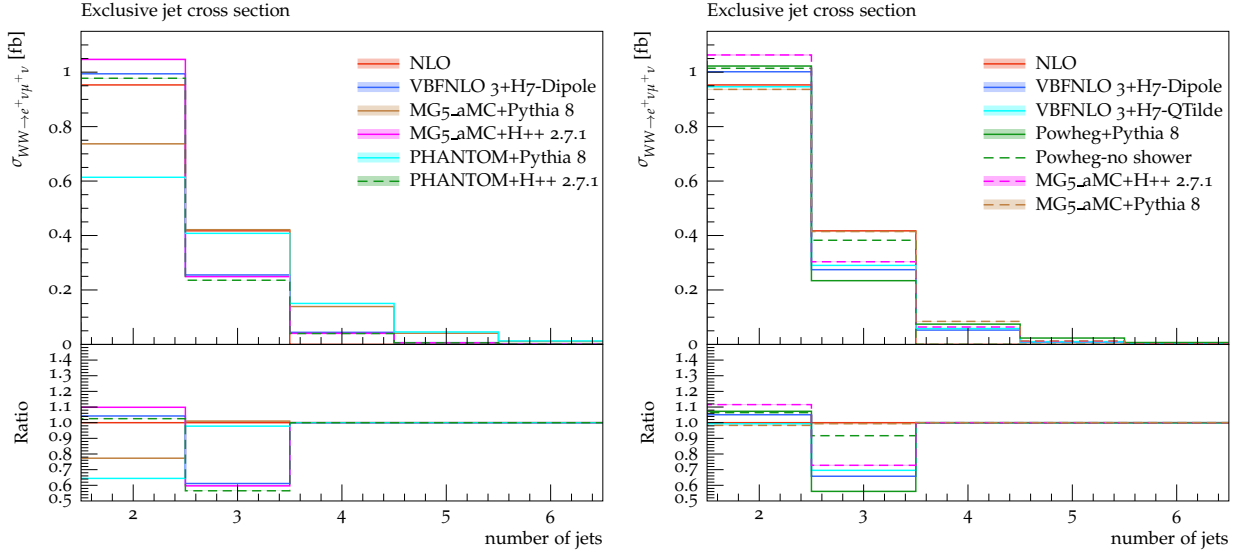


Fig. 14: Exclusive jet multiplicity from predictions matched to parton shower, at LO (left) or NLO (right) accuracy, compared with the fixed-NLO result computed with VBFNLO

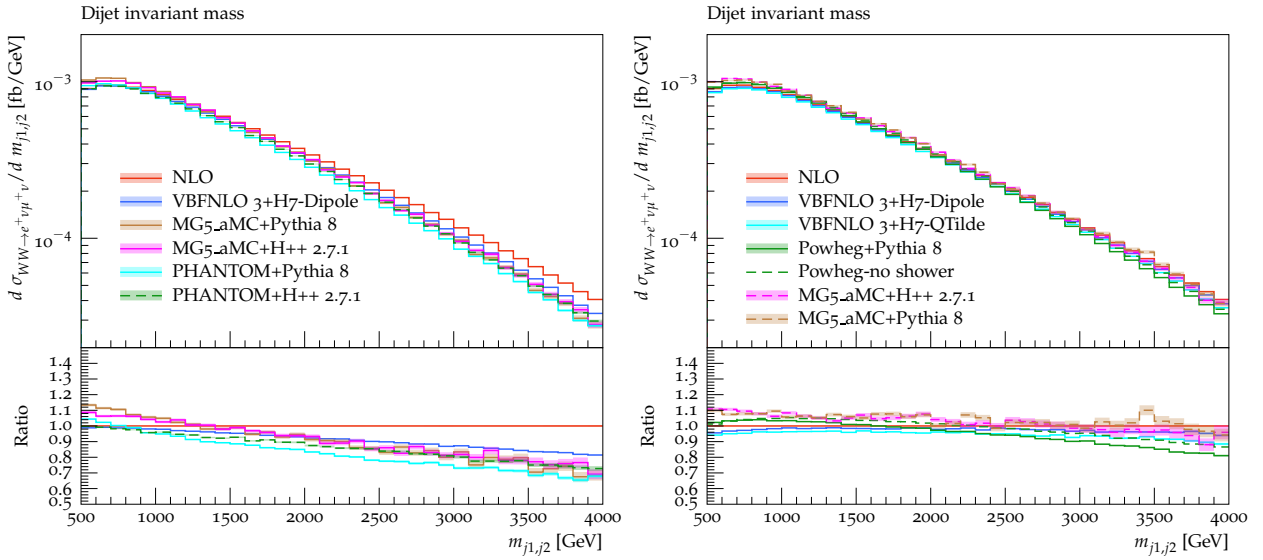


Fig. 15: Same as in Fig. 14, for the invariant mass of the two tagging jets.

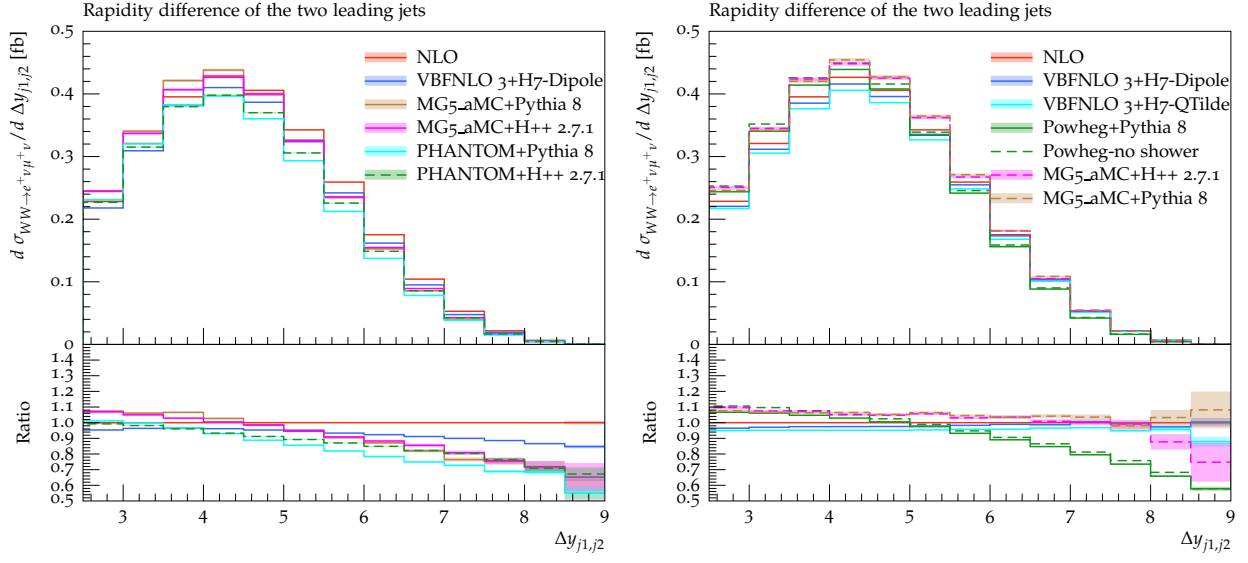


Fig. 16: Same as in Fig. 14, for the rapidity separation of the two tagging jets.

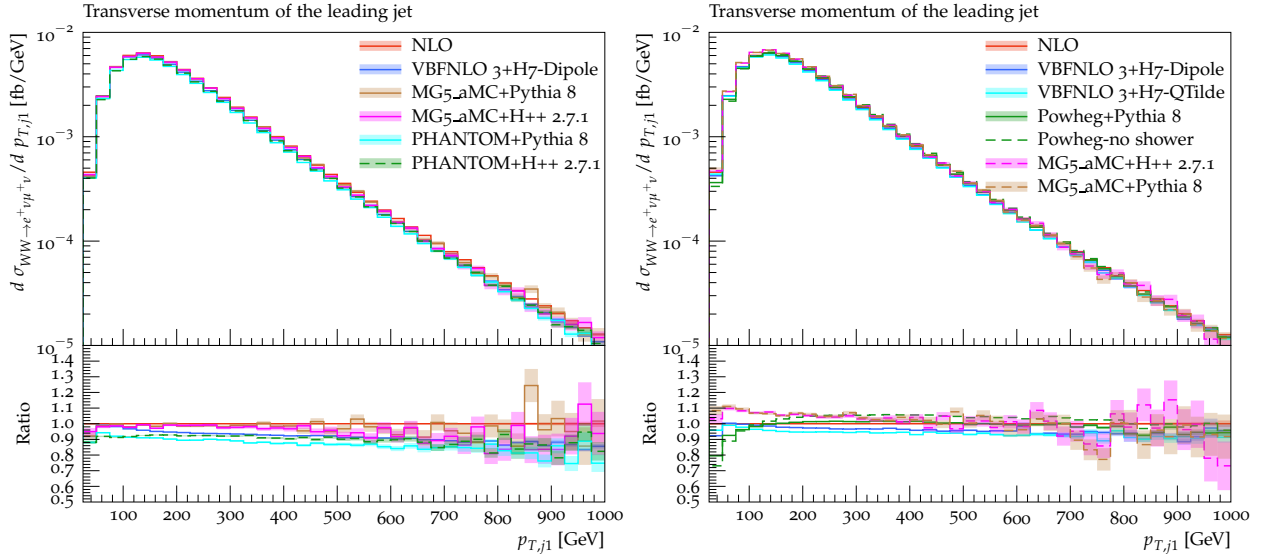


Fig. 17: Same as in Fig. 14, for the transverse momentum of the hardest jet.

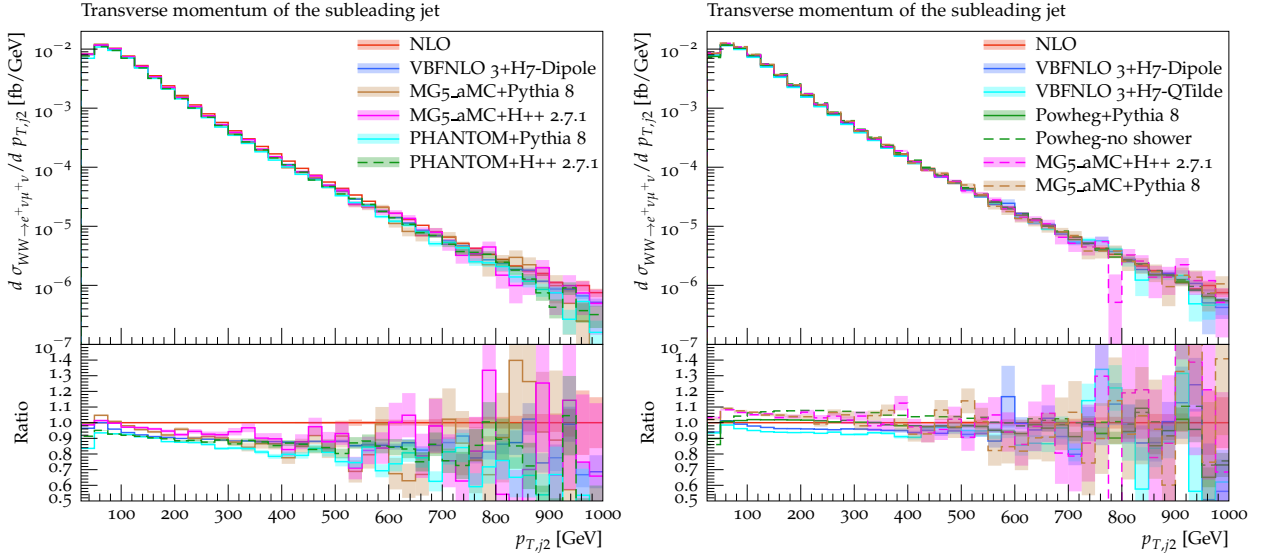


Fig. 18: Same as in Fig. 14, for the transverse momentum of the second-hardest jet.

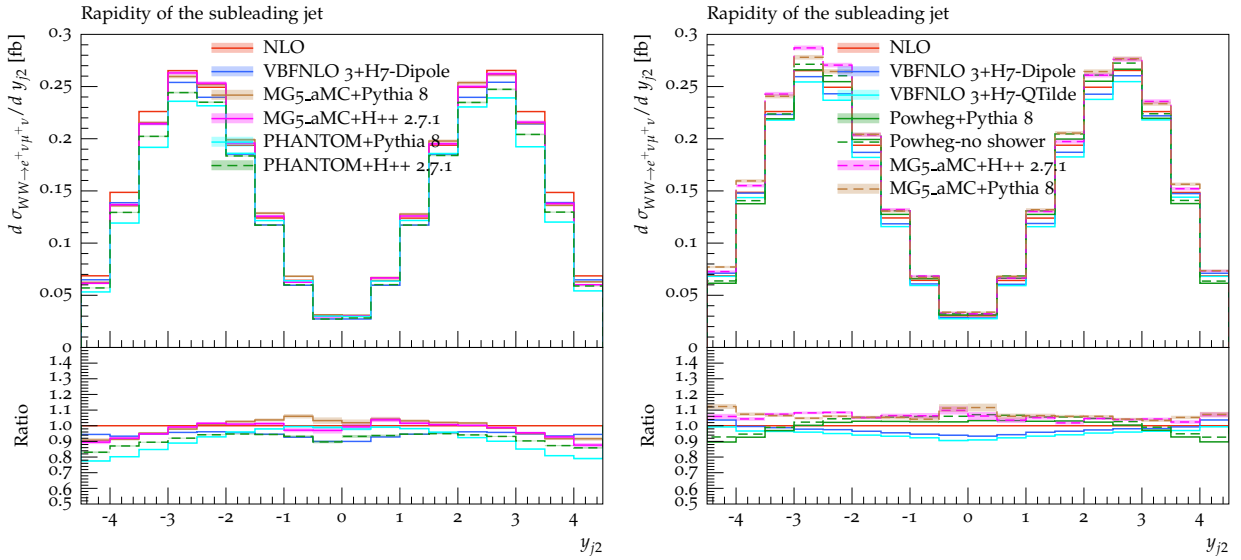


Fig. 19: Same as in Fig. 14, for the rapidity of the second-hardest jet.

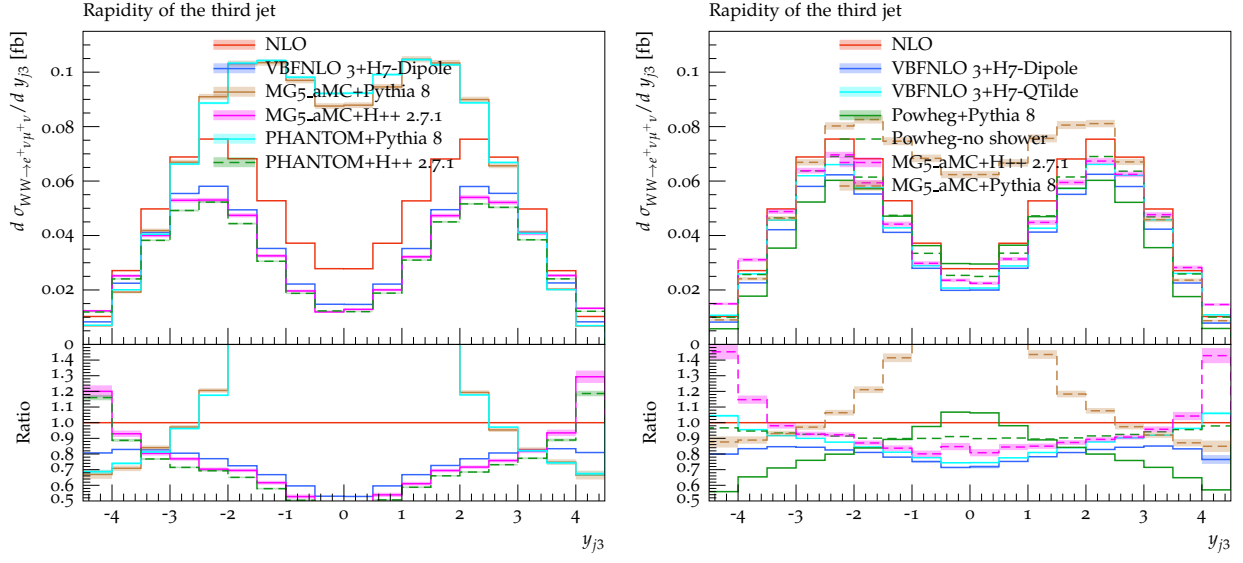


Fig. 20: Same as in Fig. 14, for the rapidity of the third-hardest jet.

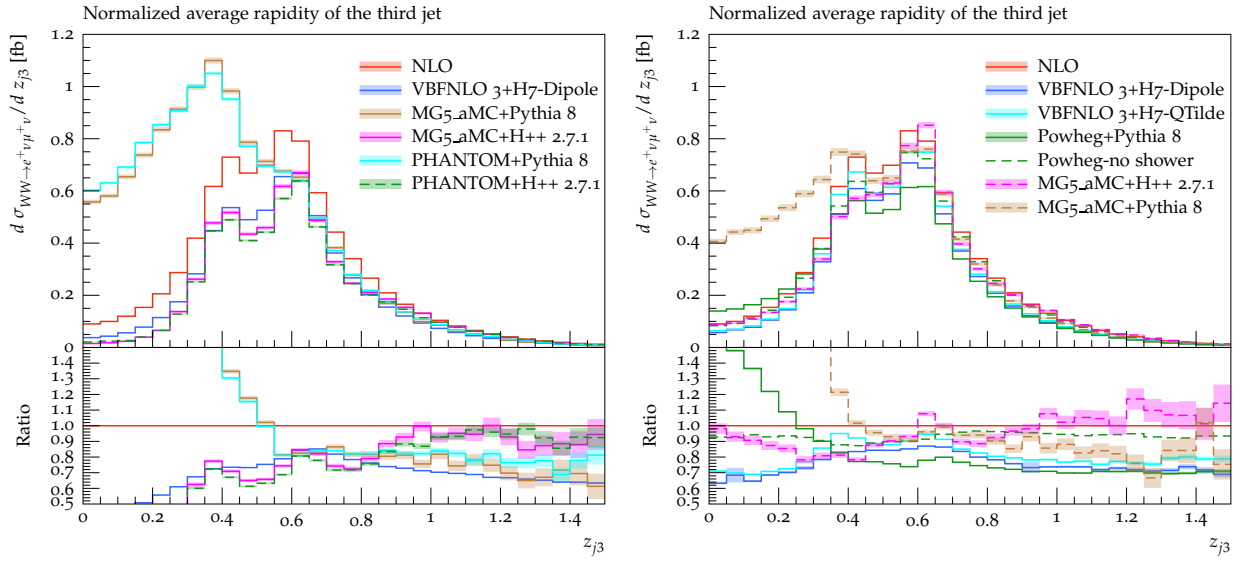


Fig. 21: Same as in Fig. 14, for the z variable of the third-hardest jet.